



HAL
open science

The nucleus acts as a ruler tailoring cell responses to spatial constraints

A. J Lomakin, C. J Cattin, D. Cuvelier, Z. Alraies, M. Molina, G. P F Nader, N. Srivastava, P. J Saez, J. M Garcia-Arcos, I. y Zhitnyak, et al.

► To cite this version:

A. J Lomakin, C. J Cattin, D. Cuvelier, Z. Alraies, M. Molina, et al.. The nucleus acts as a ruler tailoring cell responses to spatial constraints. *Science*, 2020, 370 (6514), pp.eaba2894. 10.1126/science.aba2894 . hal-03036279

HAL Id: hal-03036279

<https://hal.science/hal-03036279>

Submitted on 2 Dec 2020

HAL is a multi-disciplinary open access archive for the deposit and dissemination of scientific research documents, whether they are published or not. The documents may come from teaching and research institutions in France or abroad, or from public or private research centers.

L'archive ouverte pluridisciplinaire **HAL**, est destinée au dépôt et à la diffusion de documents scientifiques de niveau recherche, publiés ou non, émanant des établissements d'enseignement et de recherche français ou étrangers, des laboratoires publics ou privés.

Title: The nucleus acts as a ruler tailoring cell responses to spatial constraints

Authors: A.J. Lomakin ^{1,2,3*†#}, C.J. Cattin ^{4,10†}, D. Cuvelier ^{3§}, Z. Alraies ^{3,5§}, M. Molina ^{2,10}, G.P.F. Nader ³, N. Srivastava ³, P.J. Saez ^{3,10}, J.M. Garcia-Arcos ³, I.Y. Zhitnyak ^{3,6}, A. Bhargava ⁵, M.K. Driscoll ⁷, E.S. Welf ⁷, R. Fiolka ⁷, R.J. Petrie ⁸, N.S. De Silva ⁵, J.M. González-Granado ⁹, N. Manel ⁵, A.M. Lennon-Duménil ⁵, D.J. Müller ^{4*}, M. Piel ^{3*#}

Affiliations:

¹St. Anna Children's Cancer Research Institute (CCRI), CeMM Research Center for Molecular Medicine, Austrian Academy of Sciences (ÖAW), and Ludwig Boltzmann Institute for Rare and Undiagnosed Diseases, Vienna, Austria.

²King's College London, School of Basic and Medical Biosciences, Centre for Stem Cells and Regenerative Medicine, London, UK.

³Institut Curie and Institut Pierre Gilles de Gennes, PSL Research University, CNRS, UMR 144, Paris, France.

⁴ETH Zurich, Department of Biosystems Science and Engineering, Basel, Switzerland.

⁵Institut Curie, PSL Research University, INSERM, U 932, Paris, France.

⁶N.N. Blokhin Medical Research Center of Oncology, Moscow, Russia.

⁷University of Texas Southwestern Medical Center, Department of Cell Biology and Lyda Hill Department of Bioinformatics, Dallas, TX, USA.

⁸Drexel University, Department of Biology, Philadelphia, PA, USA.

⁹LamImSys Lab, Departamento de Fisiología, Facultad de Medicina, Universidad Autónoma de Madrid (UAM) and Instituto de Investigación Hospital 12 de Octubre (imas12), Madrid, Spain.

¹⁰Present addresses: F. Hoffmann-La Roche Ltd., Basel, Switzerland (C.J.C.); Institute for Bioengineering of Catalonia (IBEC), The Barcelona Institute of Science and Technology (BIST) and University of Barcelona, Barcelona, Spain (M.M.); and University Medical Center Hamburg-Eppendorf, Department of Biochemistry and Molecular Cell Biology, Hamburg, Germany (P.J.S.).

*Correspondence to: alexis.lomakin@ccri.at,

daniel.mueller@bsse.ethz.ch,

matthieu.piel@curie.fr

†These authors contributed equally to the experimental part of this work.

§These authors contributed equally to this work during the revision process.

#These authors jointly supervised this work.

Abstract: The microscopic environment inside a metazoan organism is highly crowded. Whether individual cells can tailor their behavior to the limited space remains unclear. Here, we found that cells measure the degree of spatial confinement using their largest and stiffest organelle, the nucleus. Cell confinement below a resting nucleus size deforms the nucleus, which expands and stretches its envelope. This activates signaling to the actomyosin cortex *via* nuclear envelope stretch-sensitive proteins, upregulating cell contractility. We established that the tailored contractile response constitutes a nuclear ruler-based signaling pathway involved in migratory cell behaviors. Cells rely on the nuclear ruler to modulate the motive force enabling their passage through restrictive pores in complex three-dimensional (3D) environments, a process relevant to cancer cell invasion, immune responses and embryonic development.

One Sentence Summary: Nuclear envelope expansion above a threshold triggers a contractile cell response and thus acts as a ruler for the degree of cell deformation.

Main Text:

INTRODUCTION:

Much like modern day engineered devices, cells in the human body are able to make measurements. For example, epithelial cells in the intestine monitor local cell densities, and exit the tissue above a threshold density, preventing hyperplasia (1). Immune cells can estimate the pore size of surrounding tissues to choose the site of least mechanical resistance for migration (2). Epidermal stem cells use the amount of the extracellular matrix (ECM) available for cell attachment and spreading as a guidance cue in their cell fate decision-making (3). These examples illustrate the sensitivity of complex cell behaviors to environmental spatial and mechanical constraints, known in quantitative sciences as boundary conditions (BCs) (4). Although the importance of BCs in cell physiology is increasingly recognized, only a few mechanisms by which cells can measure specific BCs are precisely identified (e.g. the stiffness of the substrate on which cells grow (5), or the geometry of their adhesive environment (6)). Amongst the known mechanisms, most are related to either strain (deformation) or stress (forces) and are collectively referred to as mechanotransduction pathways (7).

Here, we asked whether cells are also equipped with a mechanism to measure absolute dimensions, which could instruct them about distances between neighboring cells or matrix pore size. In our previous study, we discovered that many histologically unrelated cell types change their migratory strategies in response to the specific confinement height (8). This almost universally leads to a long-lasting increase in actomyosin contractility and amoeboid cell propulsion in the absence of specific adhesion to the substrate. Together with similar findings in early zebrafish embryos (9), these observations illustrate the simplest case in which cells measure one of their dimensions to adapt their behavior to local BCs *in vitro* and *in vivo*. However, the mechanism underlying this phenomenon remained unknown.

RESULTS:

Cells detect their height and trigger contractile responses below a threshold height

To tackle this question, we applied a reductionist approach in which the degree of cell confinement is precisely controlled and paralleled with quantitative microscopy. We confined single nonadherent, initially rounded, interphase cells using an ion beam-sculpted flat silicon microcantilever (Fig. 1A) mounted on an atomic force microscopy (AFM) setup (10) and

simultaneously monitored the actomyosin cytoskeleton dynamics and contractile force generation employing confocal videomicroscopy and AFM-based force spectroscopy.

Using the cell line HeLa-Kyoto (human cervical carcinoma) expressing MYH9-GFP (myosin IIA), we performed confinement experiments in which the height of the same single cell is changed in a step-wise fashion starting from 20 μm (average nonconfined cell diameter is $20 \pm 4 \mu\text{m}$, $n = 100$ cells). We found that upon reaching a specific confinement height, cells begin responding to it by steadily increasing force with which they push against the confining cantilever (6 to 5 μm confinement in Fig. 1A). Each cell had its own trigger height at which it generates the force response (Fig. 1A right graph). Most cells remained insensitive to 10 μm confinement (which corresponds to half of the initial cell height, Fig. 1B), while almost 100% of analyzed cells displayed the response upon reaching 5 μm confinement (Fig. 1A right graph). We thus chose to systematically study the response of cells to 5 vs. 10 μm confinement height.

Our analyses showed that cell confinement to 5 but not 10 μm stimulates rapid (2.05 ± 0.33 min, $n = 10$ cells) recruitment of myosin II (further referred to as myosin) from the cytosol to the cortex (Fig. 1C,D, Fig. S1A and Movie S1), which is then followed by cell cortex contraction and force production (Fig. 1E). Both phenomena required myosin activity (Fig. 1D,E) and culminated in a sustained (up to several hours) and active non-apoptotic plasma membrane (PM) blebbing (Movie S2), whose degree is directly proportional to cortical myosin concentration (Fig. S1B-D). Measuring cell blebbing index in several other primary and immortalized cell lines under different confinement heights confirmed the generality of our observations (Fig. S1E). To test whether cells would also adapt their cortical actomyosin contractility to the degree of environmental confinement in a context more closely recapitulating *in vivo* settings, we examined human fibrosarcoma cells HT1080 infiltrating 3D cell-derived matrices (CDM) (Fig. 1F). Cortical recruitment of myosin in these cells linearly scaled with self-imposed smallest dimension of the cell (Fig. 1F), thus validating our AFM-based observations. Importantly, switching cells back to the initial unconfined state in our AFM experiments induced a rapid (3.78 ± 0.94 min, $n = 7$ cells) re-localization of myosin to the cytosol (Fig. S1F), indicating that persistent contractility required a sustained confinement below the threshold height. Collectively, these experiments showed that single cells can sense the difference between 10 and 5 μm and trigger a sustained, yet reversible, active contractile response at a specific height.

Cell height-specific contractile responses depend on nuclear envelope/endoplasmic reticulum-mediated signals

We next performed experiments to narrow down the range of potential mechanisms involved in this height-dependent contractile response. Confinement experiments on adherent, well-spread cells showed qualitatively the same threshold-like response as we established for rounded nonadherent cells (Fig. S2A-C). Moreover, experimental manipulations of extracellular $[\text{Ca}^{2+}]$ or $[\text{Mn}^{2+}]$ to modulate engagement of integrins during cell contact with the surface of the confining cantilever (11) did not affect the response in nonadherent suspended cells (Fig. S2D). This suggested that the sensing mechanism does not depend on classical integrin-based mechanotransduction pathways. The sustained increase in contractility (Fig. S1D), and the fact that the response was dependent on the confinement height *per se* rather than the speed of confinement (Fig. S3), renders unlikely a signal originating from strain in the actin cortex or the PM, because these structures dissipate stress in minutes due to fast turnover (12). A natural candidate that matches the range of relevant confinement heights at which the response is triggered and that can display long-term stress due to slow turnover of its stiff elastic shell is the cell nucleus

(13). Indeed, the nucleus, and more specifically its envelope, has been shown in the recent years to trigger diverse cell responses when the nuclear compartment is deformed: entry of the transcription factors YAP/TAZ (14), activation of the ATR kinase (15), release of calcium (16), activation of the calcium-dependent phospholipase cPLA2 (17) and nuclear envelope (NE) rupture accompanied by DNA damage (18). Considering that the response to confinement was reversible and required only a few minutes for its manifestation, potential changes at the level of cell transcription/translation are unlikely at play, which we confirmed experimentally by acutely inhibiting the processes of transcription and translation (Fig. S4A). Blocking the ATR kinase activity did not yield a phenotype either (Fig. S4B). Moreover, ruptures of neither the NE nor the PM were observed at 5 μm confinement (Fig. S4C,D), excluding a mechanism based on an extracellular signal influx through transient holes in the PM, or mixing of cytoplasmic and nuclear contents.

We thus performed a small pharmacological inhibitors screen, targeting mechanotransductive pathways compatible with a minute timescale response of cells to confinement (Table S1). The screen (Fig. 2A and Table S2) showed that extracellular calcium, PM-associated stretch-sensitive channels and PM tension are not involved in the response to confinement. However, intracellular calcium, intracellular stretch-sensitive calcium channels associated with the perinuclear endoplasmic reticulum (ER), the calcium-dependent myosin light chain kinase MLCK and the NE tension sensor cPLA2 were required for the contractile response, pointing to a signal emanating from the perinuclear ER and/or the NE to activate actomyosin contraction at a specific confinement height. Consistently, imaging of intracellular calcium using the GCaMP6 calcium biosensor revealed a strong increase in cytosolic calcium upon 5 μm confinement (Fig. S5A), which was inhibited by blocking intracellular stretch-sensitive calcium channels InsP3Rs with 2APB (Fig. S5B), but not *via* chelation of extracellular calcium with BAPTA (Fig. S5A). Conversely, adding ionomycin (to artificially increase cytosolic calcium concentration) or the signaling lipid arachidonic acid/ARA (an omega-6 fatty acid that can be produced in a NE stretch-sensitive manner *via* enzymatic activity of cPLA2 on nuclear membranes (17)) to cells confined to 10 μm induced persistent blebbing without further confinement (Fig. S5C). Finally, analysis of the supernatant of a population of confined cells (using a microfabricated confinement device, see Materials and Methods) showed an increase in ARA production upon 5 μm confinement, which is lost upon cPLA2 inhibition with AACOCF3/AA (Fig. S5D). Importantly, unlike Y27632 that globally perturbed basal cell contractility at both 10 and 5 μm , the drugs yielding a phenotype in our mini-screen exerted their effect only at 5 μm , as follows from our measurements of cortical cell tension, cell pressure, and myosin cortex-to-cytosol ratio at 10 μm (Fig. S5E). This indicated that the targets of the drugs become functionally engaged in a trigger-like fashion when the cell is confined below 10 μm . These results, together with the controls for drugs activity (Fig. S5F), suggested that the nuclear membrane compartment, continuous with the perinuclear ER, might be involved in measuring the cell dimensions and triggering the contractile response below a specific confinement height.

The trigger height for contractile cell responses is determined by NE tension

To understand how the NE/perinuclear ER and associated signaling pathways could be engaged in triggering the sustained contractile response of cells to a specific confinement height, we decided to characterize nuclear shape and deformation state at 20, 10 and 5 μm confinement (Fig. 2B). We observed that the nuclear volume undergoes only very minor changes, while projected surface area of the nucleus increases substantially between 10 and 5 μm confinement

(Fig. 2C), suggesting a potential expansion of the NE. Indeed, we found that the NE in rounded nonadherent cells displays large folds and wrinkles, which become less prominent at 10 μm and completely disappear at 5 μm (Fig. 2D). To characterize this phenomenon quantitatively, we estimated the NE folding index by measuring the excess of perimeter of the NE (EOP_{NE}) in the same single cell at various heights or statistically comparing this parameter across populations of cells confined to a specific height. We found that EOP_{NE} decreases as cells get more confined (Fig. 2D; we also confirmed this result using an additional metric – standard deviation of the local curvature along the NE perimeter (Fig. S5G)). Un-confining cells led to a rapid refolding of the envelope concomitant with the loss of the contractile response (Fig. 2E). These measurements suggested that within the range of confinement heights applied in our experiments, the nucleus maintains a constant volume by progressively unfolding its envelope until reaching a fully unfolded state at 5 μm . A higher degree of confinement and more severe nuclear compression results in a significant nuclear volume loss (reported previously based on micropipette aspiration experiments (19)) and eventually NE rupture events that become predominant below 3 μm confinement height (20).

As the NE fully unfolds, it is likely to reach a state in which it stretches and becomes tensed. To estimate this parameter, we first measured the thermally and actively driven fluctuations of the NE on the time scale of seconds (see Materials and Methods and (21)). We found that the amplitude of the fluctuations systematically decreases as cells get more confined (Fig. 2F), consistent with an increase in the NE tension. Imaging nuclear pores in the NE of the same cell at various heights showed that confinement from 10 to 5 μm causes neighboring nuclear pores to become more distant from each other, consistent with a stretching of the NE (Fig. 2G). Finally, we observed that the mKate2-tagged phospholipase cPlA2, sensing lipid crowding in the NE (17), remains in the nucleoplasm at 10 μm , but relocalizes to the NE at 5 μm (Fig. 2H), a transition previously shown to be triggered by nuclear membrane tension increase and to correspond to cPLA2 enzyme activation (17). Overall, these observations suggested that confinement to 5 μm stretches the NE.

To assess whether the height threshold at which cells display the active contractile response coincides with the induction of NE stretching, we took advantage of the variety of nuclear shapes and folding states in the cell population and systematically investigated these parameters along with contractile force and cell morphology readouts. First, correlative recording of F-actin and the NE (Fig. 3A bottom images) enabled us to observe that NE unfolding temporally precedes the onset of the contractile response (Fig. 3A top graph; Movie S3), with a delay of 38 ± 17 s ($n = 20$ cells). This is compatible with a causal link between the NE unfolding-stretching and the onset of a sustained contractile response. Second, we found that cells with more folded nuclei before confinement (larger EOP_{NE}) start to contract at a lower confinement height (Fig. 3B), indicating that the degree of NE folding sets the sensitivity threshold for the ability of cells to discriminate between different confinement heights.

Because we utilized cultured proliferating cells in our experiments, a source of cell-to-cell variability in responses to confinement could come from the cell cycle stage, which introduces a natural range of NE states in a cell population (21). Therefore, we decided to test a FUCCI HeLa cell line expressing fluorescent cell cycle stage markers in our confinement experiments. We determined that unconfined G_1 cells have significantly higher values of EOP_{NE} compared to G_2 cells (Fig. S5H). While the unconfined cell height and mechanical state (basal cortical tension and cell pressure) at 10 μm confinement were similar for rounded, nonadherent G_1 and G_2 cells (Fig. S5H), G_2 cells required less confinement than G_1 cells to trigger the contractile response (Fig. S5H).

bottom right graph). This result further confirmed that the state and size of the nucleus defines a ruler to trigger the active contractile cell response. It also suggested that the nuclear ruler might render proliferating cells more or less sensitive to deformations depending on their cell cycle stage.

The ‘Nuclear Ruler’ working model

5 Altogether, our results suggested the following working model (Fig. 3C): each single cell in the rounded state has a certain nuclear volume and an excess of NE surface area stored in NE folds. When one of the dimensions of the cell is reduced below the resting nuclear diameter, the nucleus deforms and its envelope unfolds. Once the NE reaches full unfolding, it stretches, potentially together with the perinuclear ER, leading to calcium release from internal stores and
 10 cPLA2 re-localization onto the stretched NE followed by the cPLA2 enzyme activation and production of ARA. Both calcium ions and ARA are classical second messenger molecules with a well-known stimulatory effect on actomyosin contractility (22–24), thus mechanistically linking the cell height to cell contractility. Consistent with this model, the correlative live recording of cPla2-mKate2, calcium (GCaMP6-EGFP), and forces during cell height change from 10 to 5 μm ,
 15 showed re-localization of cPla2 within 20 seconds and intracellular calcium increase within less than a minute, both phenomena preceding the contractile response of the cell (Fig. S5I).

A first direct prediction of the nuclear ruler model is that as cells start squeezing through a tissue opening with a size smaller than a resting nuclear diameter, they should deform-unfold-and-stretch their nuclei. This would lead to an increase in cortical myosin concentration. To test this
 20 prediction in a controlled and quantitative manner, we microfluidically flowed HeLa cells through microchannels with bottleneck constrictions. We found that nuclear deformations reflected in changes of the nuclear roundness index, indeed, precede myosin accumulation at the cortex, and that this takes place when the nuclear diameter is changed to approximately 5, but not 10 μm (Fig. 4A). To examine whether these dependencies can be observed in spontaneously migrating cells in
 25 a more physiological context, we looked at invasive HT1080 cells maneuvering through a 3D CDM. Plotting myosin cortical accumulation against the PM excess of perimeter (i.e. cell blebbing and thus contractility measure), we verified that our measure of myosin recruitment at the cell cortex is a good predictor of the degree of cell contractility in 3D (Fig. S6). This parameter scaled with the extent of nuclear surface folding, which in turn was dependent on the smallest nuclear
 30 dimension (Fig. 4B). These data showed that both imposed and spontaneous nuclear deformations observed in migrating cells correlate with the contractile response, suggesting that the nuclear ruler could be relevant in physiological contexts such as cells circulating in blood capillaries or cells migrating through dense tissues.

Cells without the nucleus show defective contractile responses to spatial confinement

35 A second prediction of our working model is that removing the cell nucleus should affect the contractile response to confinement. We thus produced cytoplasts by cell enucleation using centrifugation (25). This resulted in a mixed population of enucleated cytoplasts and nucleated cells (Fig. 5A). Cytoplasts on average had a smaller volume compared to nucleated cells (Fig. S7A) but a rather similar height (cell volume scales to the cubic root of cell diameter). Thus, we
 40 were able to compare nucleated cells and enucleated cytoplasts of similar initial heights confined to 10 and 5 μm . While nucleated cells showed the expected contractile response at 5 μm , this was not the case for enucleated cytoplasts (Fig. 5B and Movie S4). Cytoplasts were not deficient in the contractile response pathway, because confining them further down to 1 μm triggered both a force response and myosin recruitment at the cortex (Fig. S7B), although to a significantly lesser extent

compared to nucleated cells at 5 μm . Moreover, while the response of cytoplasts was reduced upon treatment with 2APB inhibiting calcium release from internal stores, it was not affected by treatment with the cPLA2 inhibitor AACOCF3 (Fig. S7B). This suggested that the pathway triggered at 1 μm in cytoplasts could be different from that activated in nucleated cells at 5 μm . Such pathway might involve direct compression of other endomembranes (e.g. the ER that remained present in enucleated cytoplasts (Fig. S7C)).

To further demonstrate the difference in responsiveness to confinement provided by the nucleus *vs.* the rest of the cell, we used spread nucleated cells and took advantage of the small size of the wedged cantilever tip to apply a local deformation on the cell (Fig. 5C). This experiment showed that locally compressing the cell cortex in the lamellar region, even down to less than 1 micron (Fig. S8 and Movie S5), produces only a very transient response, while confining the part of the cell that contains the nucleus results in a sustained contractile response (Fig. 5D and Movie S6). Upon nuclear deformation, myosin cortical recruitment occurred even in the region which was not directly confined (Fig. 5D). This showed that the contractile response is not due to the cell deformation *per se*, but rather due to a signal which could get released locally and propagate away from the nucleus (indeed, the increase in contractility in the non-confined part manifested with a slight delay compared to the nuclear region, Movie S6). In conclusion, consistent with our working model, the nucleus is required to set the size at which the contractile response is triggered and the deformation of nuclear or nucleus-associated compartments is necessary to trigger the sustained response.

Cells with altered NE properties have a defective nuclear ruler

We further tested the nuclear ruler model by affecting the stiffness and the folded state of the NE. Lamin A/C-depleted cells (Fig. S9A) displayed nuclear dysmorphia and a more floppy NE (Fig. 6A), but did not undergo excessive cell death, even upon confinement to 5 μm height (Fig. S9B), at which the depleted cells also show a high rate of NE ruptures (Fig. 6A bottom left graph). This mechanical instability of the NE, together with the modifications of NE viscoelastic properties upon lamin A/C depletion, could contribute to the relaxation of tension in the envelope. While volume, projected area (Fig. S9C), and surface folding (Fig. S9D) of Lamin A/C-depleted nuclei were not significantly affected, we found that NE fluctuations in the depleted cells did not decrease in response to 20-10-5 μm confinement (Fig. 6A top right graph), which was in contrast to control cells (Fig. 2F). This suggested that the envelope of depleted nuclei remained floppy at all confinement heights. Confinement of depleted cells to 5 μm did not trigger intracellular calcium release nor did it increase levels of ARA production (Fig. S9E ‘5 μm confinement’ subpanel). Consistently, while their basal mechanics were unaltered at 10 μm (Fig. S9E ‘10 μm confinement’ subpanel), the depleted cells displayed an attenuated contractile response at 5 μm confinement (Figs. 6A bottom right graph and S9F). This was in agreement with the nuclear ruler model. It further suggests that the level of lamin A/C, which varies to a great extent in different cell types and environmental conditions, can modulate the response of cells to spatial confinement by affecting the mechanical properties of the NE.

The inner nuclear membrane and ER membrane protein lamin B receptor/LBR is known to control NE folding in a dose-dependent manner (26). Its overexpression leads to perinuclear ER expansion and overproduction of NE membranes, which in turn provides additional NE surface area to accommodate excess membrane protein (27, 28). Indeed, our measurements of nuclear surface folding showed that LBR-GFP overexpressing (OE) cells have a highly folded nucleus and fail to unfold it in response to 5 μm confinement, which is in contrast to LAP2/LAP2b-expressing

(control) cells (Fig. 6B images and top graph and Fig. S9G). Consistently, LBR OE abrogated both cytoplasmic calcium increase and levels of ARA production at 5 μm (Fig. S9H '5 μm confinement' subpanel). While their basal cortical mechanics were unaltered at 10 μm (Fig. S9H '10 μm confinement' subpanel), LBR-GFP OE significantly impaired contractile responses to 5 μm confinement (Figs. 6B bottom graph and S9I). Therefore, we concluded that NE folding-and-unfolding constitutes a key element of the nuclear ruler mechanism. These findings further suggested that modulation of NE components that affect the extent of NE folding (e.g. LBR and SUN2 (29)) could allow different cell types to trigger responses to various levels of confinement, or to measure different ranges of sizes, depending on their function.

10 **The nuclear ruler participates in adaptive modulation of cell propulsion during confined migration**

We hypothesized that the nuclear ruler mechanism can be used by migrating cells to increase their propulsion when surrounding space becomes limited, explaining the switch to fast amoeboid migration upon confinement of slow mesenchymal cells, which we reported previously (8). In support of this hypothesis, we found that single HeLa-Kyoto cells, remaining under the confining AFM cantilever for prolonged periods of time, can spontaneously initiate movement enabling the cells to evade the cantilever (Fig. S10A). We also observed the predicted increase in migration speed upon confinement of immature mouse bone marrow-derived dendritic cell (iDC) populations using our microfabricated confiner device (Fig. 7A, (30)). This speed increase was lost upon functional ablation of cPLA2 (Figs. 7A bottom graph, S10B upper right graph, and 7B right graph) or lamin A (Fig. 7A bottom graph, (31)), and corresponded specifically to the confinement height (3 μm) at which iDC nuclei get fully unfolded (Fig. 7C). Consistently, myosin accumulated at the iDC cortex in a cPLA2-dependent manner specifically at 3 μm (Fig. 7D). A large fraction of iDCs at 3 μm switched to a migratory polarized cell shape phenotype characteristic of fast-moving cells that was almost entirely lost upon cPLA2 depletion (Figs. 7B, S10B, and Movie S7). Overall, the data obtained from both HeLa-Kyoto cells and primary iDCs suggested that the nuclear ruler pathway could be involved in triggering a contractile 'evasion reflex' helping invasive cells to either rapidly escape or penetrate the most confined regions of dense tissues.

To further test the function of the nuclear ruler in invasive cell migration, we assessed the protease-independent ability of human metastatic skin melanoma cells (MCs), a well-established cellular model employing contractility-driven, amoeboid invasive motion *in vivo* (32), to chemotactically transmigrate (Fig. S10C) through 3D dermal collagen gels or synthetic polycarbonate membranes with different porosity. 3D collagen lattices (Fig. 8A left images) displayed pore sizes ranging from 1 to 12 μm (Fig. S10D), thus representing a heterogeneous, mechanically restrictive environment in which cells are expected to deform their nuclei. Indeed, perturbations targeting the nuclear ruler pathway affected the efficiency of MC transmigration through 3D collagen (Fig. 8A right graph and Table S3). Consistent with the diameter of their nuclei (11 ± 2 μm , $n = 100$ cells), MCs were dependent on basal actomyosin contractility or pathways associated with the nuclear ruler only when transmigrating through 8- but not 12- μm pores of polycarbonate membranes (Fig. 8B left images and Fig. S10E, and Table S3). These results suggested that thanks to the nuclear ruler, migratory cells can utilize the energetically costly actomyosin contractility motor on demand, when local cell environment becomes restrictive to migration.

45 **DISCUSSION**

Collectively, our data establish a nongenetic function for the nucleus as an internal ruler. Relying on this ruler, cells can measure the degree of their environmental confinement and rapidly tailor specific behaviors to adapt to the confinement at timescales shorter than changes in gene expression. In the context of cell migration, such tailored cellular behaviors might help cells avoiding environmental entrapment, which is relevant to cancer cell invasion, immune cell patrolling of peripheral tissues, and progenitor cell motility within a highly crowded cell mass of a developing embryo (33). The nuclear ruler mechanism defines an active function for the nucleus in cell migration, potentially explaining why enucleated cells show a poor motile capacity in dense collagen gels (34). Engaging the nuclear ruler and generating propulsive forces, cells can push their large nucleus through small openings, thus overcoming the rate-limiting effect of the bulky and stiff nucleus on confined migration. However, some highly specialized and short-lived cells such as neutrophils trade nuclear size and stiffness for uncompromised migration through dense tissue regions. To achieve this, maturing neutrophils transcriptionally upregulate LBR and downregulate LMNA expression that makes the nucleus highly pliable (35) and might cancel its rate-limiting effect and ruler function in the context of confined migration.

The nuclear ruler mechanism relies on NE tension sensing by the phospholipid-hydrolyzing enzyme cPLA2 (13, 17). The enzymatic activity of cPLA2 is fundamental to the eicosanoid biosynthetic pathway known for its function as an essential mediator of paracrine inflammatory signaling in the immune system, with effects on immune cell contractility and migration (36, 37). The function we propose here relies on a direct mechanical activation of cPLA2 and subsequent release of ARA, but it does not exclude the induction of the downstream signaling associated with ARA metabolism. When we confined the nucleus in only one cell out of a pair of closely juxtaposed cells, we did not observe any signs of contractility activation in the neighboring cell (Fig. S11), suggesting that paracrine signaling might not be enough to activate contractility in this case. Fully characterizing the signaling cascade triggered by mechanical activation of the cPLA2 pathway and subsequent changes in lipid metabolism in the context of confined cell migration is an important perspective for future studies. We also showed that the nuclear ruler pathway depends on stretch-activated intracellular calcium release. Here, we pinpointed a role for InsP3Rs, but there are many other stretch-sensitive calcium channels on the ER and nuclear membranes (38) that could contribute to the pathway in a cell type- or context-specific fashion.

Establishing the nucleus as an internal ruler of the extracellular environment opens up avenues of research not only in the field of single cell migration, but also tissue homeostasis and developmental biology. Indeed, morphological changes associated with cell spreading on the ECM are known to affect nuclear morphology and cell cycle progression (39). Therefore, the nuclear ruler might contribute to cell fate choices during tissue growth. Given that cell crowding in tissues such as epithelia alters the cell shape and aspect ratio, tissue cells in addition to the known mechanisms (1) might utilize the nucleus as a sensor of local cell density.

Materials and Methods

Cell Culture

Human cervical adenocarcinoma cells HeLa-Kyoto stably expressing myosin IIA (MYH9)-GFP and LifeAct-mCherry or MYH9-GFP and the plasma membrane-targeting CAAX box fused to mCherry, or LAP2/LAP2b-GFP, NUP107-GFP, HeLa (CCL-2) cells stably expressing cPla2-mKate2, human fibrosarcoma cells HT1080 expressing GFP-myosin light chain 2 and RFP-NLS, primary human foreskin fibroblasts (HFFs), human melanoma cells A375P, *N-rasV12* oncogene-

transformed rat liver epithelial cells IAR-2, and canine kidney epithelial cells MDCK-2 were maintained in DMEM/F12 supplemented with 10% FBS (Invitrogen) at 37°C and 5% CO₂. Human epidermal stem cells (HESCs) were cultured as previously described (40). All cell lines were tested for mycoplasma contamination using MycoScope™ PCR Mycoplasma Detection Kit (Genlantis).
 5 Mouse bone-marrow derived immature dendritic cells (iDCs) were obtained by culturing bone marrow cells (from both male and female 8- to 10- week-old LifeAct-GFP mice (41), MYH9-GFP mice (42), and control (JAX™ mice stock number: 000664) or *Lmna* KO mice (31) for 10-11 days in complete DC medium (IMDM medium supplemented with fetal calf serum (FCS, 10%), glutamine (20 mM), penicillin-streptomycin (100 U/mL), β-mercaptoethanol (50 μM) and granulocyte-macrophage colony-stimulating factor/GM-CSF (50 ng/mL)-containing supernatant obtained from transfected J558 cells.

Transfection procedure, expression vectors, and siRNA oligonucleotides

Cells were transfected with plasmid DNA using Lipofectamine™ LTX reagent (Invitrogen) transiently or stably, according to manufacturer's protocol. For RNA interference experiments,
 15 cells were transfected with siRNA oligonucleotides using Lipofectamine® RNAiMAX reagent (Invitrogen), according to manufacturer's protocol. In experiments on cPLA2a knockdown in bone marrow-derived mouse immature dendritic cells (iDCs), the cells were transfected using the Amaxa mouse Dendritic Cell Nucleofector Kit (Lonza).

The following expression vectors were used for plasmid DNA transfections: empty vector pEGFP-C1 (Clontech); Addgene plasmids: 61996 LBR pEGFP-N2 (646) (43), 40753 pGP-CMV-GCaMP6s (44), 86849 pBOB-EF1-FastFUCCI-Puro (45). To knockdown LMNA or cPLA2a, cells were transfected with nontargeting siRNA (control) or validated ON-TARGETplus SMARTpool siRNA reagents (Dharmacon) targeting human-specific *LMNA* mRNA (cat. # L-004978-00-0005), human-specific *PLA2G4A* mRNA (cat. # L-009886-00-0005), or mouse-specific *Pla2g4a* mRNA (cat. # L-063167-01-0010). Unless stated otherwise, cells were analyzed
 25 72 h post-transfection using standard Western blot or immunofluorescent analysis protocols. Based on quantitative densitometry of proteins, the knockdown efficiency was estimated as $84.7 \pm 2.5\%$ (3 repeats). Additionally, lentiviral transductions were performed to achieve lamin A knockdown in HeLa cells. Viral particles were produced by transfection of 0.8 million 293FT cells with 3 μg DNA and 8 μl TransIT-293 (Mirus Bio) per well. For shRNA mediated knockdown of lamin A, 0.4 μg CMV-VSVG, 1 μg psPAX2 and 1.6 μg of either pLKO.1-puro-LMNAsh4 (TRCN0000061837, target sequence GCCGTGCTTCCTCTCACTCAT) or pLKO1puro-shLACZ (target sequence GCGATCGTAATCACCCGAGTG) as negative control were combined. Viral supernatants were harvested 48 hours post transfection, filtered at 0.45 μm and added on to HeLa
 30 cells that had been seeded one day prior to transduction at a 2:1 ratio of viral supernatant:medium containing protamine at a final concentration of 1 μg/mL. Cells were washed once in PBS and passaged at 48 hours post transduction with 2 μg/mL of puromycin for selection of stably transduced cells.

Drug treatments

40 The following pharmacological inhibitors and chemical compounds were used: 10 μM ROCK-mediated contractility inhibitor Y27632 (Y27) (EMD), 10 μM myosin II ATPase inhibitor blebbistatin (BBS) (Toronto Research Chemicals), 20 μM Ca²⁺-sensitive myosin light chain kinase/MLCK inhibitor ML-7 (Sigma-Aldrich), 1 mM apoptosis inducer hydrogen peroxide (H₂O₂), 1 μM transcription inhibitor triptolide (TRP) (Tocris Bioscience), 50 μg ml⁻¹ translation

inhibitor cycloheximide (CHX) (Sigma-Aldrich), 1 μ M AZD6738 inhibiting the Serine/Threonine protein kinase Ataxia Telangiectasia and Rad3 related (ATR) capable of sensing nuclear envelope tension (Tocris Bioscience), 10 μ M nonspecific plasma membrane permeability marker propidium iodide (PI) (Sigma-Aldrich), 0.4 mM plasma membrane tension reducer sodium deoxycholate (DOCL) (Sigma-Aldrich), 10 μ M gadolinium (III) chloride (Gd^{3+}) or 5 μ M peptide GsMTx4 from the tarantula venom affecting mechanosensitive ion channels on the plasma membrane (Tocris Bioscience), 2 mM extracellular Ca^{2+} chelator BAPTA (Sigma-Aldrich), 10 μ M intracellular Ca^{2+} chelator BAPTA-AM (Sigma-Aldrich), 10 μ M ionomycin (IOM) directly facilitating the transport of Ca^{2+} across the plasma membrane (Sigma-Aldrich), 70 μ M signaling lipid arachidonic acid (ARA) (a product of enzymatic activity of the nuclear envelope stretch-sensitive enzyme cPLA2) activating actomyosin contractility (Cayman Chemical), 20 μ M AACOCF3 (AA) or 10 μ M PACOCF3 (PA) inhibiting the nuclear envelope stretch-sensitive enzyme cPLA2 (Tocris Bioscience), 100 μ M 2APB or 10 μ M Xestospongine C (Xesto) blocking stretch-activated inositol triphosphate receptors (InsP3Rs) on the ER/nuclear membranes (Tocris Bioscience), and 20 μ M broad-spectrum matrix metalloproteinase inhibitor GM6001 (Merck Millipore). Growth medium was supplemented with 1% DMSO (vol/vol) (Sigma-Aldrich) in control experiments.

Western blotting

Cells were collected and resuspended in Laemmli buffer. Proteins were separated using sodium dodecyl sulfate polyacrylamide gel electrophoresis (SDS-PAGE) and transferred onto PVDF membranes. After incubation with primary (Lamin A/C antibody #2032 (Cell Signaling Technology), cPLA2a antibody #PA5-29100 (Invitrogen), and GAPDH antibody #ab9483 (Abcam)) and secondary (IRDye® and VRDye™ (LI-COR)) antibodies, the membranes were visualized using Odyssey® CLx Infrared Imaging System (LI-COR).

Quantitative PCR (qPCR)

To assess the efficacy of the siRNA treatment, qPCR was carried out on iDCs after 48 hours of the siRNA treatment. RNA extraction was performed using RNeasy Micro RNA kit (Qiagen), according to the manufacturer's protocol. cDNA was produced using the high capacity cDNA synthesis kit (Thermo Fisher), according to the manufacturer's protocol, starting from 1 μ g of RNA. Quantitative PCR experiments were performed using Taqman Gene Expression Assay (Applied Biosystems) and carried out on a Lightcycler 480 (Roche) using the settings recommended by the manufacturer. The following primers were used: Mm01284324_m1 for PLA2g4 and Mm99999915 for GAPDH as a control. cPLA2a expression was assessed in si-control and si-cPLA2a iDCs. Samples were run in triplicate for each condition. Data were subsequently normalized to GAPDH values, and to the values obtained in control iDCs. The fold change was calculated using the formula $2^{-\Delta\Delta CT}$.

Single-cell flat AFM-based confinement coupled to live cell imaging

Trypsinized cells were resuspended in CO₂-independent, phenol red-free DMEM/F-12 medium supplemented with 10% FBS (Invitrogen) and plated on glass-bottomed 35-mm dishes (FluoroDish, WPI). Experiments with non-adherent cells were initiated 30 minutes after cell plating to allow for cell sedimentation. Spread cells were obtained 6 hours post cell plating. Dishes with cells were mounted in a dish heater (JPK Instruments) and kept at 37 °C under an inverted light microscope (Axio Observer.Z1; Zeiss) equipped with a confocal microscope unit (LSM 700; Zeiss) and atomic force microscopy (AFM) head (CellHesion 200; JPK Instruments).

5 Focused ion beam (FIB)-sculpted, flat silicon microcantilevers were processed and calibrated as described in (46). The microcantilevers were fixed on a standard JPK glass block and mounted in the AFM head. The cantilever was lowered on the cell to a preset height with a constant speed of $0.5 \mu\text{m}\cdot\text{s}^{-1}$, and the resulting varying force and cantilever height were recorded over time. At the same time, differential interference contrast (DIC) and fluorescence images at the midplane of the confined cell (the imaging settings were readjusted to the medial plane of the cell each time the cell was confined to a specific height) were recorded every 5 seconds using a $63\times$ water immersion objective. All microscopy equipment was placed, and experiments were carried out in a custom-made isolation box.

10 Determination of cell pressure and cortical tension

Cell geometry, pressure, and cortical tension were measured based on AFM and imaging data as described in (46) and (47).

Production of cytoplasts

Enucleated cells were generated as described in (25) and (48).

15 Microfabrication-based confinement of cell populations

To obtain large quantities of confined cells for cell population or biochemical studies, cell confinement was performed using a home-made device (8) consisting of a suction cup made in polydimethylsiloxane (PDMS, RTV615, GE) used to press a confining coverslip bearing PDMS microspacers (micropillars) on top of the culture substrate populated with cells. The height of the micropillars ($10 \mu\text{m}$ vs. $5 \mu\text{m}$) determines the height for spatial confinement of cells between the coverslip and the substrate. A version of the cell confiner adapted to multi-well plates was used to perform multiple experiments in parallel (20). The molds for the PDMS micro-spacers were fabricated following standard photolithography procedures. The surface of the confining side was always treated with non-adhesive pLL-PEG (SuSoS).

25 Assaying activation of apoptosis in live cells

To detect levels of active apoptotic caspases, the Image-iT LIVE Red Poly Caspases detection kit based on a fluorescent inhibitor of caspases (FLICA) methodology (I35101, Molecular probes) was used according to the manufacturer's protocol.

Biochemical measurements of arachidonic acid (ARA) release

30 Cells were confined using microfabricated devices as described in the subsection "Microfabrication-based confinement of cell populations". Confinement was released and the cells were immediately extracted with Dole's solution (heptane, isopropyl alcohol, 1 N sulfuric acid; 10:40:1). Pentafluorobenzyl esters of the fatty acids were prepared and quantified by gas chromatography-mass spectrometry with reference to an internal standard of $d8$ -AA as described in (49).

Epithelial monolayer stretching

A custom-made stretching device was used to perform epithelial monolayer stretching experiments as described in (1).

Chemotactic transmigration assays

Serum-starved A375P cells were harvested and transferred in serum-free medium to the upper compartment of 5, 8 (Cat. # 3421 and 3428, Corning), or 12 (Cat. # CBA-107, Cell Biolabs Inc.) μm -pore polycarbonate membrane inserts (transwells). Cell density was adjusted according to the specific area of each transwell with 5×10^4 , 1.5×10^5 , and 7.5×10^5 cells added to 5, 12, and 8 μm transwells, respectively. Cells were allowed to transmigrate toward the lower compartment containing 10% FBS for 12 h. Transmigration efficiency was calculated as number of cells at the lower compartment divided by the number of cells added to the upper compartment of a transwell.

To examine the ability of A375P cells to chemotax through 3D collagen gels, atelopeptide fibrillar bovine dermal collagen (Cat. # 5005-B; PureCol, Advanced BioMatrix) was prepared at 1.7 mg ml^{-1} in DMEM and allowed to polymerize in the upper compartment of the 12 μm -pore polycarbonate membrane insert (Cat. # CBA-107, Cell Biolabs Inc.). Serum-starved cells were seeded on top of the collagen pad in serum-free medium, allowed to adhere and transmigrate through the collagen layer and the membrane toward the lower compartment containing 10% FBS for 24 h. Transmigration efficiency was calculated as number of cells at the lower compartment divided by the number of cells added to the upper compartment of the transwell.

Generation of 3D cell-derived matrices (CDMs)

HFFs were plated at high density on gelatin-coated and glutaraldehyde-treated 35 mm (4×10^5 cells, MatTek) or 50 mm (5.7×10^5 cells, Warner Instruments) glass-bottom dishes. Cultures were maintained for 10 days, adding new media with $50 \mu\text{g/ml}$ ascorbic acid every other day. The matrices were denuded of cells by adding extraction buffer (20 mM NH_4OH and 0.5% Triton X100 in PBS) for 10 min at room temperature and washed with PBS.

Quantitative image analysis

Fluorescence intensity levels (mean gray values, a.u.) were obtained from background subtracted images using the ImageJ/Fiji software (NIH, <http://rsb.info.nih.gov/ij/index.html>).

The Imaris (version 8.3) image analysis software (Bitplane) was utilized to measure nuclear volume reconstructed from 3D confocal microscopy images.

The dimensionless parameter excess of perimeter (EOP) was calculated to estimate the amount of nuclear envelope (NE) or plasma membrane (PM) area stored in macro- and micro-folds. To calculate EOP, we first obtained values for perimeter (P) and surface area (A) from 2D images taken at the maximum radius of the nucleus (NE marker LAP2-GFP labelling) or cell (PM marker CAAX box-mCherry labelling). Next, we introduced R_0 as the radius of the circle defined by the area A, which allowed us to compute EOP as the ratio between $(P - 2\pi R_0)$ and $(2\pi R_0)$. EOP values of a highly folded object tend to be close to 1, while EOP of an object with a smooth surface tend to be close to 0. Additional theoretical calculations were performed to account for experimentally observed changes in nuclear aspect ratio (AR); no significant contribution of AR changes to the measured values of EOP was observed.

Nuclear roundness index was obtained using the shape descriptors tool in ImageJ/Fiji.

The MIPAR™ v.3.2.3. image analysis software (MIPAR Software) and the Kappa plugin for ImageJ/Fiji (<https://github.com/brouhardlab/Kappa/tree/master/docs#fit-the-curve-to-the-data>) were used to estimate NE surface curvature.

To measure NE fluctuations, nuclei of live cells expressing LAP2-GFP were recorded using a high frame rate acquisition mode (250 msec/frame) for 5 minutes. The position of each nucleus was

corrected for linear and rotational drift using the Stackreg plugin of the ImageJ/Fiji software. Upon drift correction, the edge of the nucleus was registered at a given angle. NE fluctuations were calculated by measuring the standard deviation of the NE from its mean position. To precisely position the NE, linescans across the NE (intensities along a line of 1 pixel in width perpendicular to the NE) were made at different positions along the NE. For each point along the NE and for each timepoint in the movie, the point of maximum intensity was calculated on the linescan and a parabola was fitted on points before and after the maxima to determine the localization of the NE with a sub-pixel resolution. For each position along the NE, the mean position was taken as the mean of all the timepoints. The standard deviation of the position of the NE around this mean position was taken as one measure for the fluctuation of the NE. Each point along the NE contributes one measure. Obtained mean NE fluctuation values were expressed in μm . The same approach can be applied to measure PM fluctuations. A floppy, and thus less tensed, membrane is expected to fluctuate more, while a membrane under tension exhibits no or significantly diminished fluctuations.

The distance between neighboring nuclear pores (NP-NP distance) was estimated for the same living cell expressing a NP maker NUP107-GFP at different degrees of spatial confinement. To this end, a medial confocal slice of the nucleus was obtained to then trace individual NPs along the NE using the Linescan function of the MetaMorph (version 7.7) software (Molecular Devices). Each individual NP was resolved as a local maximum of fluorescence intensity on the Linescan diagram. The distance between nearest local maxima was represented as NP-NP distance.

Cell speed was analyzed using the manual tracking plugin of ImageJ/Fiji.

To measure collagen pore sizes, collagen fibers were imaged *via* axially swept light-sheet microscopy (50). The fibers were then detected from the deconvolved images by applying a steerable filter (51) followed by non-maximum-suppression. We then calculated pore sizes using a custom-written Matlab code implementing the algorithm described in (2).

Statistics and reproducibility of experiments

Unless stated otherwise, statistical significance was determined by two-tailed unpaired or paired Student's t-test after confirming that the data met appropriate assumptions (normality, homogenous variance and independent sampling). Statistical data are presented as average \pm either SEM or SD. Sample size (n) and *p*-value are specified in the text of the paper or figure legends. Samples in most cases were defined as the number of cells counted/examined within multiple different fields of view on the same dish/slide, and thus represent data from a single sample within a single experiment. When data from a single sample are shown, they are representative of at least three additional samples from independent experiments.

References and Notes:

1. G. T. Eisenhoffer, P. D. Loftus, M. Yoshigi, H. Otsuna, C.-B. Chien, P. A. Morcos, J. Rosenblatt, Crowding induces live cell extrusion to maintain homeostatic cell numbers in epithelia. *Nature*. **484**, 546–549 (2012).
- 5 2. J. Renkawitz, A. Kopf, J. Stopp, I. de Vries, M. K. Driscoll, J. Merrin, R. Hauschild, E. S. Welf, G. Danuser, R. Fiolka, M. Sixt, Nuclear positioning facilitates amoeboid migration along the path of least resistance. *Nature*. **568**, 546–550 (2019).
3. B. Trappmann, J. E. Gautrot, J. T. Connelly, D. G. T. Strange, Y. Li, M. L. Oyen, M. A. Cohen Stuart, H. Boehm, B. Li, V. Vogel, J. P. Spatz, F. M. Watt, W. T. S. Huck,
10 Extracellular-matrix tethering regulates stem-cell fate. *Nat. Mater.* **11**, 642–649 (2012).
4. M. D. Vahey, D. A. Fletcher, The biology of boundary conditions: cellular reconstitution in one, two, and three dimensions. *Curr. Opin. Cell Biol.* **26**, 60–68 (2014).
5. R. Oria, T. Wiegand, J. Escribano, A. Elosegui-Artola, J. J. Uriarte, C. Moreno-Pulido, I. Platzman, P. Delcanale, L. Albertazzi, D. Navajas, X. Trepap, J. M. García-Aznar, E. A.
15 Cavalcanti-Adam, P. Roca-Cusachs, Force loading explains spatial sensing of ligands by cells. *Nature*. **552**, 219–224 (2017).
6. M. Théry, A. Jiménez-Dalmaroni, V. Racine, M. Bornens, F. Jülicher, Experimental and theoretical study of mitotic spindle orientation. *Nature*. **447**, 493–496 (2007).
7. J. Z. Kechagia, J. Ivaska, P. Roca-Cusachs, Integrins as biomechanical sensors of the
20 microenvironment. *Nat. Rev. Mol. Cell Biol.* **20**, 457–473 (2019).
8. Y.-J. Liu, M. Le Berre, F. Lautenschlaeger, P. Maiuri, A. Callan-Jones, M. Heuzé, T. Takaki, R. Voituriez, M. Piel, Confinement and Low Adhesion Induce Fast Amoeboid Migration of Slow Mesenchymal Cells. *Cell*. **160**, 659–672 (2015).
9. V. Ruprecht, S. Wieser, A. Callan-Jones, M. Smutny, H. Morita, K. Sako, V. Barone, M.
25 Ritsch-Marte, M. Sixt, R. Voituriez, C.-P. Heisenberg, Cortical Contractility Triggers a Stochastic Switch to Fast Amoeboid Cell Motility. *Cell*. **160**, 673–685 (2015).
10. M. P. Stewart, Y. Toyoda, A. A. Hyman, D. J. Müller, Tracking mechanics and volume of globular cells with atomic force microscopy using a constant-height clamp. *Nat. Protoc.* **7**, 143–154 (2012).
- 30 11. F. Kong, A. J. García, A. P. Mould, M. J. Humphries, C. Zhu, Demonstration of catch bonds between an integrin and its ligand. *J. Cell Biol.* **185**, 1275–1284 (2009).
12. A. G. Clark, O. Wartlick, G. Salbreux, E. K. Paluch, Stresses at the Cell Surface during Animal Cell Morphogenesis. *Curr. Biol.* **24**, R484–R494 (2014).
13. B. Enyedi, P. Niethammer, A Case for the Nuclear Membrane as a Mechanotransducer.
35 *Cell. Mol. Bioeng.* **9**, 247–251 (2016).
14. A. Elosegui-Artola, I. Andreu, A. E. M. Beedle, A. Lezamiz, M. Uroz, A. J. Kosmalska, R. Oria, J. Z. Kechagia, P. Rico-Lastres, A.-L. Le Roux, C. M. Shanahan, X. Trepap, D. Navajas, S. Garcia-Manyes, P. Roca-Cusachs, Force Triggers YAP Nuclear Entry by Regulating Transport across Nuclear Pores. *Cell*. **171**, 1397-1410.e14 (2017).
- 40 15. A. Kumar, M. Mazzanti, M. Mistrik, M. Kosar, G. V. Beznoussenko, A. A. Mironov, M.

- Garrè, D. Parazzoli, G. V. Shivashankar, G. Scita, J. Bartek, M. Foiani, ATR Mediates a Checkpoint at the Nuclear Envelope in Response to Mechanical Stress. *Cell*. **158**, 633–646 (2014).
- 5 16. N. Itano, S. -i. Okamoto, D. Zhang, S. A. Lipton, E. Ruoslahti, Cell spreading controls endoplasmic and nuclear calcium: A physical gene regulation pathway from the cell surface to the nucleus. *Proc. Natl. Acad. Sci.* **100**, 5181–5186 (2003).
17. B. Enyedi, M. Jelcic, P. Niethammer, The Cell Nucleus Serves as a Mechanotransducer of Tissue Damage-Induced Inflammation. *Cell*. **165**, 1160–1170 (2016).
- 10 18. M. Raab, M. Gentili, H. de Belly, H.-R. Thiam, P. Vargas, A. J. Jimenez, F. Lautenschlaeger, R. Voituriez, A.-M. Lennon-Dumenil, N. Manel, M. Piel, ESCRT III repairs nuclear envelope ruptures during cell migration to limit DNA damage and cell death. *Science (80-.)*. **352**, 359–362 (2016).
19. A. C. Rowat, J. Lammerding, J. H. Ipsen, Mechanical Properties of the Cell Nucleus and the Effect of Emerin Deficiency. *Biophys. J.* **91**, 4649–4664 (2006).
- 15 20. M. Le Berre, J. Aubertin, M. Piel, Fine control of nuclear confinement identifies a threshold deformation leading to lamina rupture and induction of specific genes. *Integr. Biol.* **4**, 1406 (2012).
21. F.-Y. Chu, S. C. Haley, A. Zidovska, On the origin of shape fluctuations of the cell nucleus. *Proc. Natl. Acad. Sci.* **114**, 10338–10343 (2017).
- 20 22. F.-C. Tsai, T. Meyer, Ca²⁺ Pulses Control Local Cycles of Lamellipodia Retraction and Adhesion along the Front of Migrating Cells. *Curr. Biol.* **22**, 837–842 (2012).
23. P. Solanes, M. L. Heuzé, M. Maurin, M. Bretou, F. Lautenschlaeger, P. Maiuri, E. Terriac, M. Thoulouze, P. Launay, M. Piel, P. Vargas, A. Lennon-Duménil, Space exploration by dendritic cells requires maintenance of myosin II activity by IP3 receptor 1. *EMBO J.* **34**, 798–810 (2015).
- 25 24. Ming Cui Gong, A. Fuglsang, D. Alessi, S. Kobayashi, P. Cohen, A. V. Somlyo, A. P. Somlyo, Arachidonic acid inhibits myosin light chain phosphatase and sensitizes smooth muscle to calcium. *J. Biol. Chem.* **267**, 21492–21498 (1992).
25. V. Rodionov, E. Nadezhdina, J. Peloquin, G. Borisy, Digital fluorescence microscopy of cell cytoplasts with and without the centrosome. *Methods Cell Biol.* **67**, 43–51 (2001).
- 30 26. S. Gravemann, N. Schnipper, H. Meyer, A. Vaya, M. J. M. Nowaczyk, A. Rajab, W. K. Hofmann, B. Salewsky, H. Tönnies, H. Neitzel, H. H. Stassen, K. Sperling, K. Hoffmann, Dosage effect of zero to three functional LBR-genes in vivo and in vitro. *Nucleus*. **1**, 179–189 (2010).
- 35 27. Y. Ma, S. Cai, Q. Lv, Q. Jiang, Q. Zhang, Sodmergen, Z. Zhai, C. Zhang, Lamin B receptor plays a role in stimulating nuclear envelope production and targeting membrane vesicles to chromatin during nuclear envelope assembly through direct interaction with importin beta. *J. Cell Sci.* **120**, 520–530 (2007).
- 40 28. J. Ellenberg, E. D. Siggia, J. E. Moreira, C. L. Smith, J. F. Presley, H. J. Worman, J. Lippincott-Schwartz, Nuclear Membrane Dynamics and Reassembly in Living Cells: Targeting of an Inner Nuclear Membrane Protein in Interphase and Mitosis. *J. Cell Biol.*

- 138**, 1193–1206 (1997).
29. D. A. Donahue, S. Amraoui, F. di Nunzio, C. Kieffer, F. Porrot, S. Opp, F. Diaz-Griffero, N. Casartelli, O. Schwartz, SUN2 Overexpression Deforms Nuclear Shape and Inhibits HIV. *J. Virol.* **90**, 4199–4214 (2016).
- 5 30. M. Le Berre, E. Zlotek-Zlotkiewicz, D. Bonazzi, F. Lautenschlaeger, M. Piel, in *Methods in Cell Biology* (2014); <https://linkinghub.elsevier.com/retrieve/pii/B9780128002810000142>), pp. 213–229.
31. Y. Kim, Y. Zheng, Generation and characterization of a conditional deletion allele for Lmna in mice. *Biochem. Biophys. Res. Commun.* **440**, 8–13 (2013).
- 10 32. V. Sanz-Moreno, G. Gadea, J. Ahn, H. Paterson, P. Marra, S. Pinner, E. Sahai, C. J. Marshall, Rac Activation and Inactivation Control Plasticity of Tumor Cell Movement. *Cell.* **135**, 510–523 (2008).
33. V. Venturini, F. Pezzano, F. C. Castro, H.-M. Häkkinen, S. Jiménez-Delgado, M. Colomer-Rosell, M. M. Sánchez, Q. Tolosa-Ramon, S. Paz-López, M. A. Valverde, P. Loza-Alvarez, M. Krieg, S. Wieser, V. Ruprecht, The nucleus measures shape deformation for cellular proprioception and regulates adaptive morphodynamics. *bioRxiv* (2019), doi:10.1101/865949.
- 15 34. D. M. Graham, T. Andersen, L. Sharek, G. Uzer, K. Rothenberg, B. D. Hoffman, J. Rubin, M. Balland, J. E. Bear, K. Burrige, Enucleated cells reveal differential roles of the nucleus in cell migration, polarity, and mechanotransduction. *J. Cell Biol.* **217**, 895–914 (2018).
- 20 35. H. R. Manley, M. C. Keightley, G. J. Lieschke, The Neutrophil Nucleus: An Important Influence on Neutrophil Migration and Function. *Front. Immunol.* **9** (2018), doi:10.3389/fimmu.2018.02867.
- 25 36. P. V. Afonso, M. Janka-Junttila, Y. J. Lee, C. P. McCann, C. M. Oliver, K. A. Aamer, W. Losert, M. T. Cicerone, C. A. Parent, LTB4 Is a Signal-Relay Molecule during Neutrophil Chemotaxis. *Dev. Cell.* **22**, 1079–1091 (2012).
37. R. Majumdar, A. Tavakoli Tameh, C. A. Parent, Exosomes Mediate LTB4 Release during Neutrophil Chemotaxis. *PLOS Biol.* **14**, e1002336 (2016).
- 30 38. M. T. Alonso, J. García-Sancho, Nuclear Ca²⁺ signalling. *Cell Calcium.* **49**, 280–289 (2011).
39. J. Aureille, V. Buffière-Ribot, B. E. Harvey, C. Boyault, L. Pernet, T. Andersen, G. Bacola, M. Balland, S. Fraboulet, L. Van Landeghem, C. Guilluy, Nuclear envelope deformation controls cell cycle progression in response to mechanical force. *EMBO Rep.* **20** (2019), doi:10.15252/embr.201948084.
- 35 40. F. Watt, B. Simon, D. Prowse, in *Cell Biology* (Elsevier, 2006); <https://linkinghub.elsevier.com/retrieve/pii/B9780121647308500174>), pp. 133–138.
41. J. Riedl, K. C. Flynn, A. Raducanu, F. Gärtner, G. Beck, M. Bösl, F. Bradke, S. Massberg, A. Aszodi, M. Sixt, R. Wedlich-Söldner, Lifeact mice for studying F-actin dynamics. *Nat. Methods.* **7**, 168–169 (2010).
- 40

42. Y. Zhang, M. A. Conti, D. Malide, F. Dong, A. Wang, Y. A. Shmist, C. Liu, P. Zerfas, M. P. Daniels, C.-C. Chan, E. Kozin, B. Kachar, M. J. Kelley, J. B. Kopp, R. S. Adelstein, Mouse models of MYH9-related disease: mutations in nonmuscle myosin II-A. *Blood*. **119**, 238–250 (2012).
- 5 43. N. Zuleger, D. A. Kelly, A. C. Richardson, A. R. W. Kerr, M. W. Goldberg, A. B. Goryachev, E. C. Schirmer, System analysis shows distinct mechanisms and common principles of nuclear envelope protein dynamics. *J. Cell Biol.* **193**, 109–123 (2011).
- 10 44. T.-W. Chen, T. J. Wardill, Y. Sun, S. R. Pulver, S. L. Renninger, A. Baohan, E. R. Schreiter, R. A. Kerr, M. B. Orger, V. Jayaraman, L. L. Looger, K. Svoboda, D. S. Kim, Ultrasensitive fluorescent proteins for imaging neuronal activity. *Nature*. **499**, 295–300 (2013).
45. S.-B. Koh, P. Mascalchi, E. Rodriguez, Y. Lin, D. I. Jodrell, F. M. Richards, S. K. Lyons, A quantitative FastFUCCI assay defines cell cycle dynamics at a single-cell level. *J. Cell Sci.* **130**, 512–520 (2017).
- 15 46. C. J. Cattin, M. Duggelin, D. Martinez-Martin, C. Gerber, D. J. Müller, M. P. Stewart, Mechanical control of mitotic progression in single animal cells. *Proc. Natl. Acad. Sci.* **112**, 11258–11263 (2015).
- 20 47. E. Fischer-Friedrich, A. A. Hyman, F. Jülicher, D. J. Müller, J. Helenius, Quantification of surface tension and internal pressure generated by single mitotic cells. *Sci. Rep.* **4**, 6213 (2015).
48. V. Rodionov, E. Nadezhdina, G. Borisy, Centrosomal control of microtubule dynamics. *Proc. Natl. Acad. Sci.* **96**, 115–120 (1999).
- 25 49. D. Riendeau, J. Guay, P. K. Weech, F. Laliberte, J. Yergey, C. Li, S. Desmarais, H. Perrier, S. Liu, D. Nicoll-Griffith, I. P. Street, Arachidonyl trifluoromethyl ketone, a potent inhibitor of 85-kDa phospholipase A2, blocks production of arachidonate and 12-hydroxyeicosatetraenoic acid by calcium ionophore-challenged platelets. *J. Biol. Chem.* **269**, 15619–15624 (1994).
- 30 50. K. M. Dean, P. Roudot, E. S. Welf, G. Danuser, R. Fiolka, Deconvolution-free Subcellular Imaging with Axially Swept Light Sheet Microscopy. *Biophys. J.* (2015), doi:10.1016/j.bpj.2015.05.013.
51. F. Aguet, M. Jacob, M. Unser, in *Proceedings - International Conference on Image Processing, ICIP* (2005).

35 **Figure 1: Cells sense their own height and upregulate actomyosin contractility at a specific height.** **A:** Left, representative force curve in response to step-wise (1 μm -increment, 5 min-interval) confinement of a cell by the flat microcantilever. Right, percentage of cells displaying a sustained force increase (> 15 nN) as a function of height. **B:** 3D images (XZ views) of the same live HeLa-Kyoto cell expressing MYH9-GFP at indicated heights. **C:** Time-lapse image sequence of the same live cell (XY views; single, midplane confocal slices) at 10 μm (top) followed by height change to 5 μm (bottom). Scale bar, 10 μm . **D:** Left, representative graph of myosin cortex-to-cytoplasm ratio as a function of time in the same live cell upon 10 μm and subsequently 5 μm

confinement. Middle and right, the same ratio measured in single live cells at 10 μm and subsequently 5 μm confinement in the presence of DMSO or the ROCK inhibitor Y27632 ($n = 10$ cells per condition; p value, paired t test). Measurements were done 5 minutes after application of each confinement height. **E:** Left, representative force response curve (ΔF , force increase) as a function of time in the same live cell upon 10 μm and subsequently 5 μm confinement. Middle, statistical analysis of force response (ΔF) in cells at 10 vs. 5 μm . Right, statistical analysis of force response (ΔF) to 5 μm confinement in cells treated with DMSO or Y27632. Measurements were done 5 minutes after application of the confinement. Data are from ≥ 2 experiments (mean \pm SD; $n = 10$ cells per condition; p value, unpaired t test). **F:** Left, representative image of 3D dermal fibroblast cell-derived matrix (CDM) stained with a collagen I antibody. Middle, representative images of HT1080 cells expressing GFP-myosin light chain 2 (GFP-MLC2) in 3D CDM (XY views, single confocal slices) with the smallest cell dimension (h) measured as 10 and 5 μm . Right, self-imposed smallest cell dimensions plotted against corresponding values for myosin cortex-to-cytoplasm ratio in the cells within 3D CDM ($n = 30$ cells). Scale bar, 20 μm .

Figure 2: The height-specific contractile response is controlled by mechanisms associated with nuclear/ER membrane stretch. **A:** Cortical myosin levels (left) and force response (ΔF , right) to 5 μm confinement of HeLa-Kyoto cells treated with drugs affecting PM tension and extracellular $[\text{Ca}^{2+}]_{\text{out}}$ (blue) or ER/NE tension and intracellular $[\text{Ca}^{2+}]_{\text{in}}$ (red). See Table S1 for drug target description and Materials and Methods for drug concentrations. Data are from ≥ 2 experiments (mean \pm SD; $n = 10$ cells per perturbation; see Table S2 for statistics). **B:** 3D XZ views of the DAPI-stained nucleus at 20, 10, and 5 μm . **C:** Left, XY views of the nucleus at 10 and 5 μm . Middle and right, measurements of nuclear area and volume at 10 and subsequently 5 μm ($n = 10$ cells; p value, paired t test). Scale bar, 10 μm . **D:** Left top, images of the LAP2-GFP-labeled NE confined to 20-to-10-to-5 μm . Scale bar, 5 μm . Left bottom, zoom on a gradually opening nuclear fold. Scale bar, 2.5 μm . Right, EOP_{NE} at 10 and subsequently 5 μm (upper graph, $n = 10$ different cells; p value, paired t test) and statistics of EOP_{NE} in cell populations at 20, 10, and 5 μm (lower graph, data are from ≥ 2 experiments; mean \pm SD; $n = 30$ cells per height; p value, unpaired t test). **E:** Images of the LAP2-GFP-labeled NE and EOP_{NE} quantifications in live cells confined to 5 μm and un-confined to 20 μm ($n = 10$ cells; p value, paired t test). Scale bar, 5 μm . **F:** NE fluctuation curves at various confinement heights (h) and quantifications of NE fluctuations at 10 and subsequently 5 μm ($n = 10$ cells; p value, paired t test) or in cell populations at 20, 10, and 5 μm (mean \pm SD; $n = 30$ cells per height; p value, unpaired t test). **G:** Images of NUP107-GFP-labeled nuclear pores (NPs) and quantification of inter-NP (NP-NP) distance at 10 and subsequently 5 μm ($n = 10$ cells; p value, paired t test). Scale bar, 0.5 μm . **H:** Images of nuclear cPlax2-mKate2 signal and quantification of its NE-to-nucleoplasm (NE/NPM) ratio at 10 and subsequently 5 μm ($n = 10$ cells; p value, paired t test). Scale bar, 1.5 μm .

Figure 3: The “Nuclear Ruler” working model. **A:** Representative graph of temporal evolution of NE unfolding (EOP_{NE}, blue) and PM blebbing (EOP_{PM}, red) and time-lapse image sequence of the LAP2-GFP-labeled NE (blue) and Lifeact-mCherry-labeled F-actin (red) in the same live cell responding to the sequential confinement to 20-to-10-to-5 μm . Scale bar, 5 μm . **B:** Height for the onset of contractile force response as a function of the degree of NE folding (EOP_{NE}) before confinement ($n = 20$ cells). **C:** Sketch of the working model: cells utilize the nucleus as an internal ruler for their height. When a cell deforms below the resting height (h_1) of its nucleus, the nuclear

surface area (S) increases while the nuclear volume (V) remains constant. At a critical height (h_2), the NE fully expands and gets stretched increasing its tension (T). The increase in NE tension stimulates stretch-sensitive proteins whose activity promotes and/or reinforces cortical actomyosin contractility.

5

Figure 4: Correlation between nuclear stretching and cortical recruitment of myosin in experimentally deformed and spontaneously moving cells. **A:** Left, representative images of DAPI-stained (magenta) HeLa-Kyoto cells microfluidically pushed into bottleneck PDMS constrictions. Color-coded nuclear outlines at different time points for a cell pushed into the constriction are shown at the bottom. Middle, representative image sequence of the nucleus (magenta) and MYH9-GFP-labeled myosin (green) in a live cell pushed into the constriction. Right top and bottom, images of the nucleus inside the bottleneck constriction reaching roundness equivalent to 10 and 5 μm confinement heights, and graph of the nuclear roundness index (magenta) and myosin cortical recruitment (green) in time representative of $n = 30$ cells. **B:** Left, representative images (XY views, single confocal slices) of RFP-NLS-labeled nuclei (top) and GFP-MLC2-labeled myosin in HT1080 cells within 3D CDM. Middle, smallest nuclear dimension plotted against corresponding values of EOP_{NE} . Right, myosin cortex-to-cytoplasm ratio plotted against corresponding values of EOP_{NE} ($n = 30$ cells). Scale bar, 5 μm .

10

15

20

Figure 5: Enucleated cells and cells regioselectively confined to avoid the nucleus do not trigger contractile responses at relevant heights. **A:** Left, representative images (XY views) of a nucleated (DAPI (blue)-positive) cell and an enucleated (DAPI-negative) cytoplast. Right, XZ views of a cell and a cytoplast of similar height representative of those selected for analyses. Scale bar, 5 μm . **B:** Images (top) and quantifications (bottom) of myosin cortical accumulation (left) and force response (ΔF , right) in cells ($n = 10$) and cytoplasts ($n = 10$) confined to 10 vs. 5 μm . Data are from ≥ 2 experiments; mean \pm SD; p value, unpaired t test. Scale bar, 10 μm . **C:** Regioselective confinement of the nuclear region (lower cell) vs. the nucleus-free lamella (upper cell). Cyan, DAPI nuclear stain; Red hot, myosin signal; Dashed squares, zoomed regions (right images). Scale bar, 10 μm . **D:** Quantifications of myosin cortical accumulation and force response (ΔF) upon nuclear ($n = 10$) and lamellar cortex ($n = 10$) confinement. Data are from ≥ 2 experiments; mean \pm SD; p value, unpaired t test.

25

30

Figure 6: The nuclear ruler is defective in cells with altered nuclear envelope properties. **A:** Top left, representative images of DAPI-stained nuclei in HeLa-Kyoto cells treated with control or *LMNA* siRNA. Top right, quantifications of NE fluctuations in *LMNA* siRNA-treated cells under 20, 10, and 5 μm confinement (data are from ≥ 2 experiments; mean \pm SD; $n = 20$ cells per height; p value, unpaired t test). Bottom left, percentage of cells displaying nuclear rupture at 5 μm . Data are from ≥ 2 experiments; $n = 15$ cells per condition. Bottom right, force response (ΔF) to 5 μm confinement. Data are from ≥ 2 experiments; mean \pm SD; $n = 10$ (*Ctrl* si) and 15 (*LMNA* si) cells; p value, unpaired t test. Scale bar, 10 μm . **B:** Top, representative images of NE in HeLa-Kyoto cells stably expressing LAP2-GFP or ectopically overexpressing (OE) LBR-GFP and corresponding EOP_{NE} quantifications. Data are from ≥ 2 experiments; mean \pm SD; $n = 10$ cells per condition; p value, unpaired t test). Bottom, force response (ΔF) to 5 μm confinement. Data are

35

40

from ≥ 2 experiments; mean \pm SD; $n = 10$ (LAP2) and 15 (LBR OE) cells; p value, unpaired t test. Scale bar, 10 μm .

Figure 7: The nuclear ruler function in immune cell migration. **A:** Left and middle, cartoons illustrating primary culture of iDCs and their confinement between two parallel surfaces inducing a highly migratory DC phenotype. Right top, iDC velocity measured at 10 ($n = 20$ cells), 4 ($n = 35$ cells), and 3 ($n = 35$ cells) μm confinement height (h). Right bottom, cell velocity (v_{cell}) measured at 3 μm confinement in control (DMSO and wild-type (WT)) vs. cPLA2-inhibited (AACOCF3/AA treatment) or *Lmna* knockout (KO) cells ($n = 20$ cells per condition). Data are from ≥ 2 experiments; mean \pm SD; p value, unpaired t test. **B:** Top, temporal color-coded cell tracks from a representative time-lapse movie of control (*Ctrl* si) and cPLA2a-depleted (*Pla2g4a* si) LifeAct-GFP-expressing iDCs under 3 μm -confinement. Bottom, statistical analysis of cell velocity (v_{cell}) for control and depleted cells at 4 vs. 3 μm . Data are from ≥ 2 experiments; mean \pm SD; $n = 20$ cells per condition; p value, unpaired t test. Scale bar, 50 μm . **C:** Representative images of DAPI-stained nuclei (XY view, single confocal slices) and EOP_{NE} quantifications in iDCs at 4 vs. 3 μm . Data are from ≥ 2 experiments; mean \pm SD; $n = 35$ cells per condition; p value, unpaired t test. Scale bar, 5 μm . **D:** Representative images and quantifications of myosin cortical accumulation in control (*Ctrl* si) and cPLA2a-depleted (*Pla2g4a* si) MYH9-GFP-expressing iDCs at 4 and 3 μm . Data are from ≥ 2 experiments; mean \pm SD; $n = 20$ cells per condition; p value, unpaired t test. Scale bar, 15 μm .

Figure 8: The nuclear ruler function in cancer cell migration. **A:** Left, 3D light-sheet microscopy images of atelopeptide fibrillar bovine dermal collagen (1.7 mg ml⁻¹) lattices. Right, quantifications of the percentage of human melanoma cells A375P able to chemotactically transmigrate through the lattice (1 mm thick) in the presence of the broad-spectrum matrix metalloproteinase inhibitor GM6001 in conditions affecting cell contractility (Y27, BBS, and ML7), NE properties (*LMNA* si and LBR OE), cPLA2 expression and activity (*PLA2G4A* si, AA, and PA), and stretch-sensitive calcium release (Gd³⁺, GsMTx4, 2APB, and Xesto). Data are from ≥ 2 experiments; mean \pm SD; $n \geq 300$ cells per condition. See Table S3 for drug target description and pairwise statistical comparisons, and Materials and Methods for drug concentrations. **B:** Scanning electron microscopy images of polycarbonate membranes with 12 (blue) and 8 (red) μm pores (scale bar, 10 μm), and quantifications of the percentage of A375P cells able to chemotactically transmigrate through the pores in the conditions specified in **A**. Data are from ≥ 2 experiments; mean \pm SD; $n \geq 300$ cells per condition. See Table S3 for drug target description and pairwise statistical comparisons, and Materials and Methods for drug concentrations. Dotted line in **A** and **B**, cell transmigration rate upon global perturbation of actomyosin contractility.

Acknowledgments: The authors wish to acknowledge I. Poser and A. Hyman (Max Planck Institute of Molecular Cell Biology and Genetics, Dresden, Germany) for providing stable BAC transgenic HeLa cell lines expressing various fluorescent protein markers, as well as P. Niethammer (Sloan-Kettering Institute, New York, New York, USA) for sharing the HeLa cell line that stably expresses cPla2-mKate2, and V. Sanz-Moreno (Queen Mary University of London, London, UK) for providing A375P cells. LBR pEGFP-N2 (646) was a gift from E. Schirmer (Addgene plasmid #61996; <http://n2t.net/addgene:61996>; RRID: Addgene_61996). pGP-CMV-GCaMP6s was a gift from D. Kim & GENIE Project (Addgene plasmid # 40753;

<http://n2t.net/addgene:40753>; RRID: Addgene_40753). pBOB-EF1-FastFUCCI-Puro was a gift from K. Brindle & D. Jodrell (Addgene plasmid #86849; <http://n2t.net/addgene:86849>; RRID: Addgene_86849). We thank L. Allison and R. Fleck (Centre for Ultrastructural Imaging at King's College London, London, UK) and D. Mathys (Swiss Nanoscience Institute at University of Basel, Basel, Switzerland) for performing scanning electron microscopy of polycarbonate membranes and focused ion beam-based flat AFM cantilever nanofabrication, respectively. We are grateful to B. Baum (University College London, London, UK), D. Gerlich (Institute of Molecular Biotechnology of the Austrian Academy of Sciences, Vienna, Austria), and M. Kraakman (Children's Cancer Research Institute, Vienna Austria) for comments on the manuscript. We also thank G. Charras (University College London, London, UK) for the advice to estimate inter-nuclear pore distance in nuclei at various degrees of spatial confinement, and N. Carpi (Institut Curie, Paris, France) for excellent technical assistance with experiments. We also thank A. Williart, L. Barbier, and P. Vargas (Institut Curie, Paris, France) for performing additional experiments during the revision of the article, which were finally not included in the article but helped our reasoning. Some illustrations accompanying figures of the present manuscript were partially generated using the BioRender.com online tool; **Funding:** The research leading to these results has received funding from the People Programme (Marie Skłodowska-Curie Actions) of the European Union's Seventh Framework Programme (FP7/2007-2013) under REA grant agreement n. PCOFUND-GA-2013-609102, through the PRESTIGE programme coordinated by Campus France. A.J.L. was supported by the Marie Curie & PRESTIGE Fellowship (grant 609102), London Law Trust Medal Fellowship (grant MGS9403), and a Career Grant for Incoming International Talent (grant 875764) from the Austrian Research Promotion Agency (FFG). D.J.M. was supported by the National Center of Competence in Research (NCCR) Molecular Systems Engineering. This work was also supported by the Institut Pierre-Gilles de Gennes-IPGG (Equipment d'Excellence, "Investissements d'avenir", program ANR-10-EQPX-34) and laboratoire d'excellence, "Investissements d'avenir" program ANR-10-IDEX-0001-02 PSL and ANR-10-LABX-31. This work was additionally supported by the Institut National du Cancer (INCa grant 2018-PL Bio-02) to M.P. and INCa (grant 2019-PL BIO-07) and INSERM Plan Cancer Single Cell (grant 19CS007-00) to N.M. and M.P. R.J.P. was supported by the National Institute of General Medical Sciences of the National Institutes of Health under Award Number R01GM126054. R.F. received funding from the National Institutes of Health (grants R35GM133522-01 and R33CA235254-02). J.M.G.G. was financed by Instituto de Salud Carlos III (ISCIII) (PI17/01395; PI20/00306) and I3 SNS program. M.D. was supported by the National Institute of General Medical Sciences (grant K99GM123221). N.S.D.S. received a Marie Skłodowska-Curie Individual Fellowship (DCBIO 751735) and an EMBO Long-term fellowship (ALTF 1298-2016). I.Z. was supported by a Metchnikov Fellowship from the Franco-Russian Scientific Cooperation Program. **Author contributions:** A.J.L., C.J.C., D.J.M. and M.P. designed the project. A.J.L. and M.P. jointly supervised the project. A.J.L. and C.J.C. performed all key experiments and analyzed the data. D.C. analyzed most of force spectroscopy data and developed analytical approaches to estimate the degree of nuclear membrane folding. Z.A., G.P.F.N., P.J.S. and A.M.L-D. performed experiments with primary mouse immature dendritic cells. M.M. performed experiments with A375P cells. G.P.F.N. performed experiments with HeLa-cPla2 cells and with LaminA/C-depleted HeLa cells. N.S. performed experiments with HeLa-LAP2 cells and developed analytical approaches to estimate the degree of nuclear membrane fluctuation. J.M.G-A. and I.Z. performed western blot analysis of LMNA knockdown efficiency as well as experiments on the effect of transcription and translation inhibition in HeLa cells. J.M.G-A.

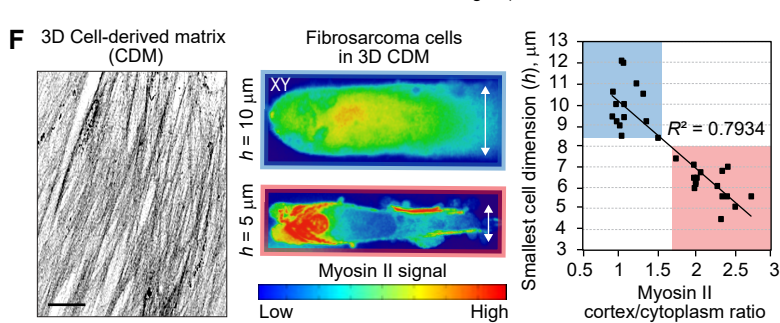
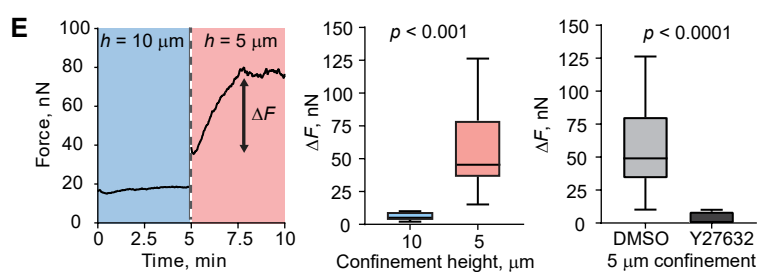
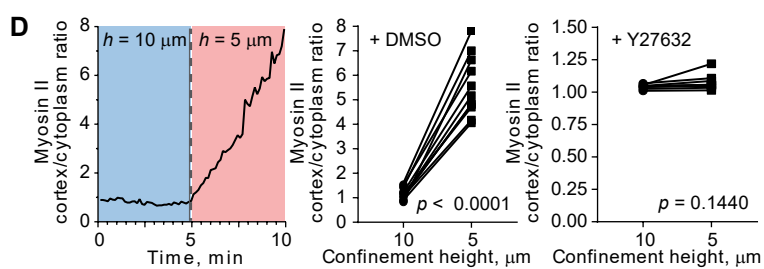
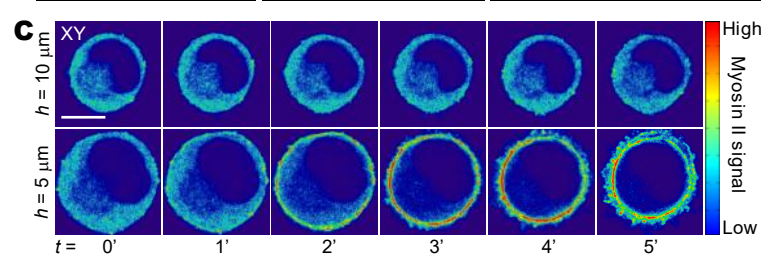
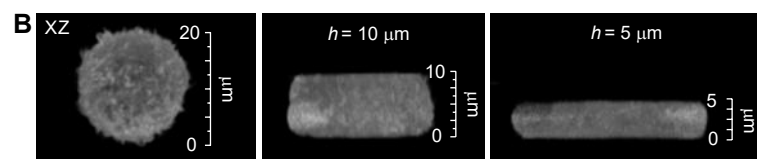
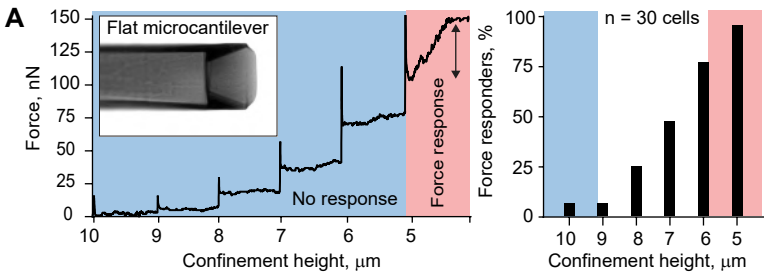
5 additionally assisted with manuscript preparation for submission. A.B. performed shRNA-mediated LMNA knockdown in HeLa cells. N.D.S. and J.M.G.G. provided *Lmna* KO DCs and mice. N.M. supervised A.B. and N.S.D.S.. M.K.D., E.S.W., and R.F. analyzed 3D collagen data. R.J.P. performed experiments with HT1080 cells in 3D CDMs. A.J.L., C.J.C., D.J.M. and M.P. wrote the manuscript. All authors discussed the results and implications, and commented on the manuscript at all stages; **Competing interests:** The authors declare no competing financial interests; and **Data and materials availability:** All data is available in the main text or the supplementary materials.

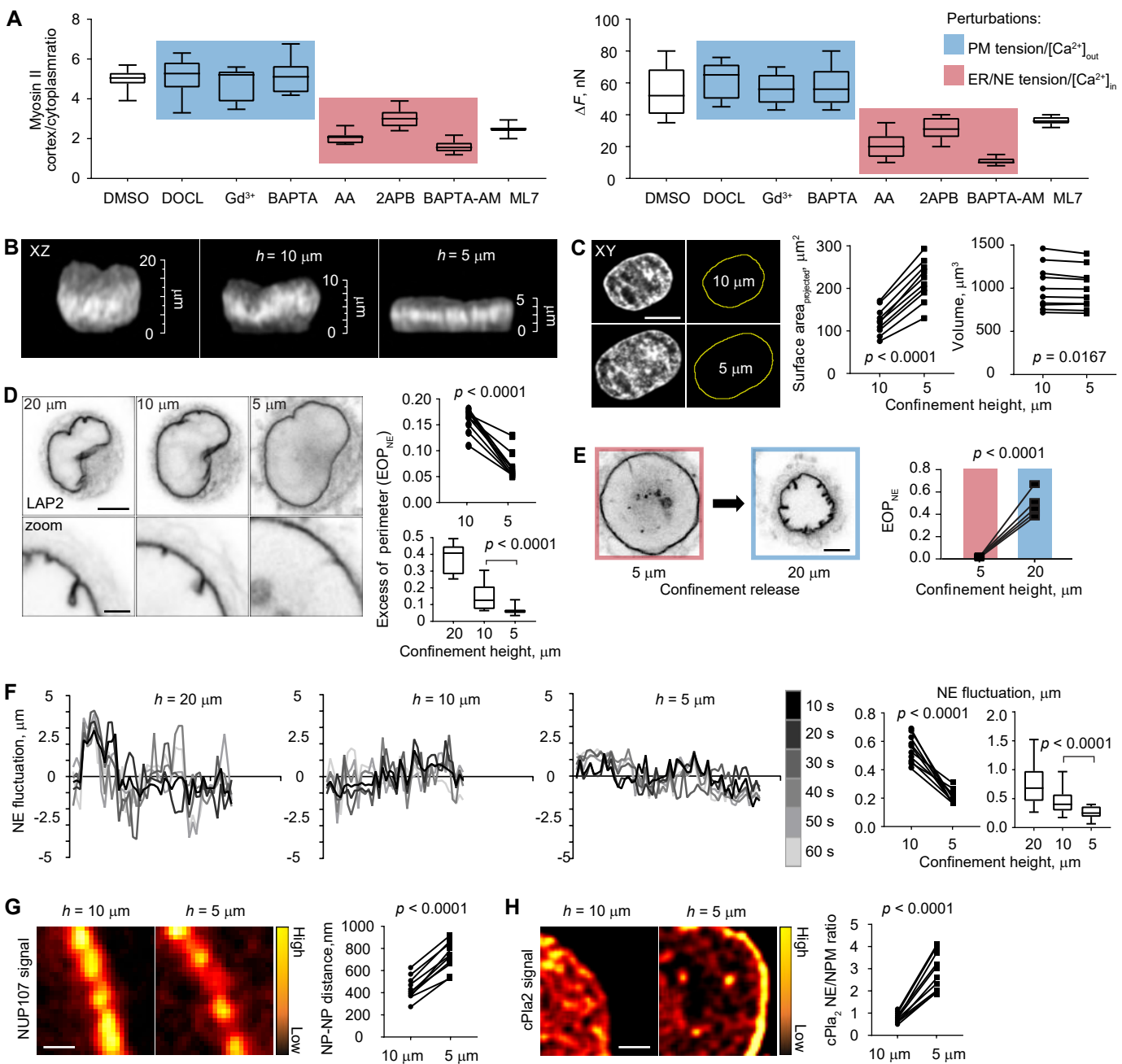
Supplementary Materials:

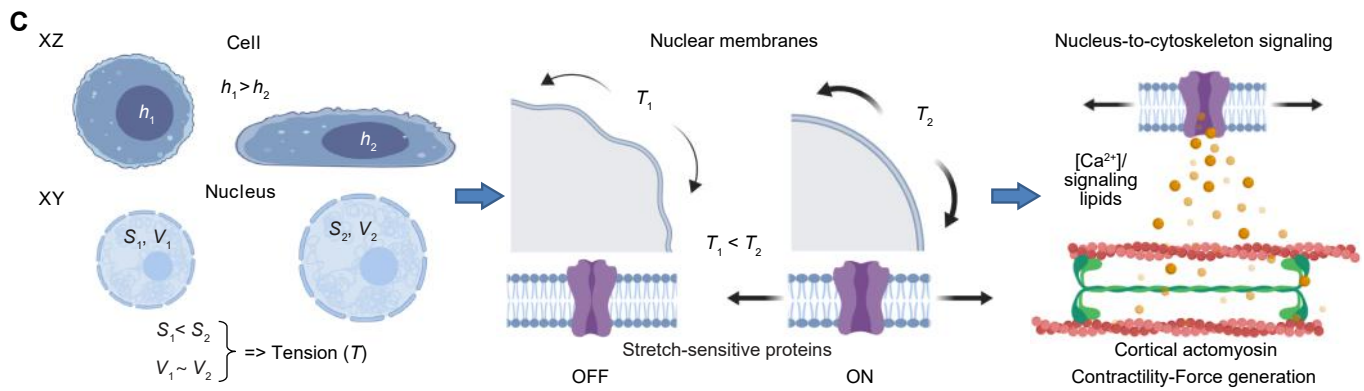
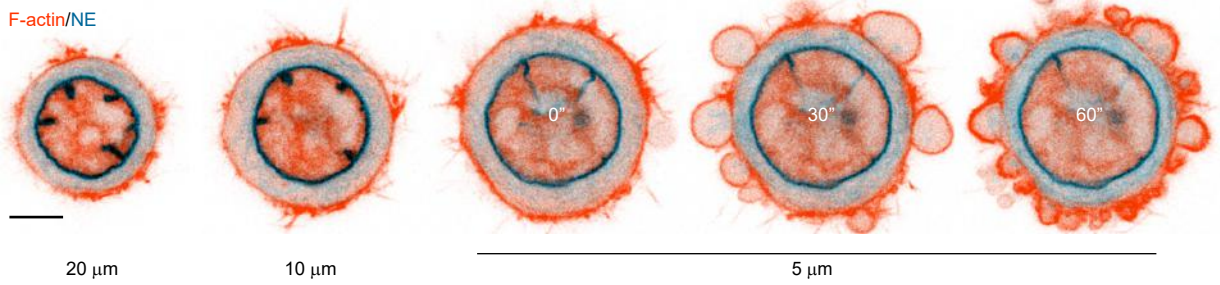
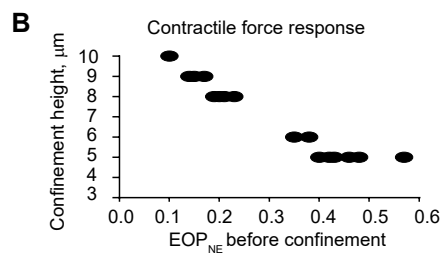
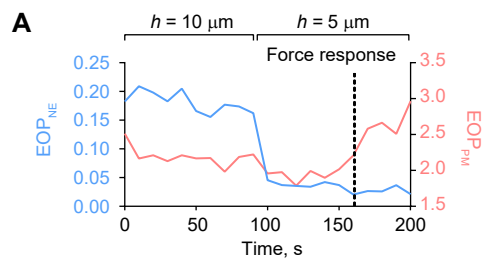
10 Figures S1-S11

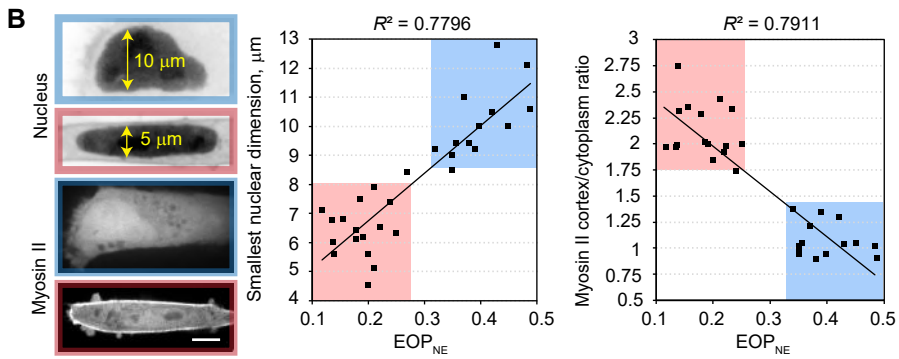
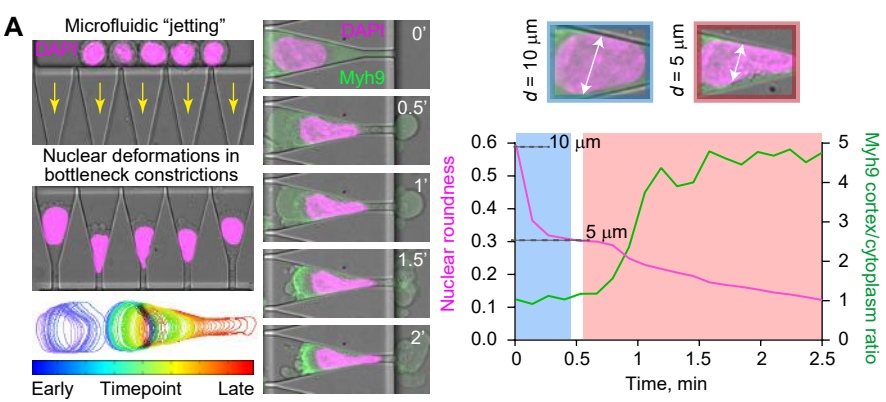
Tables S1-S3

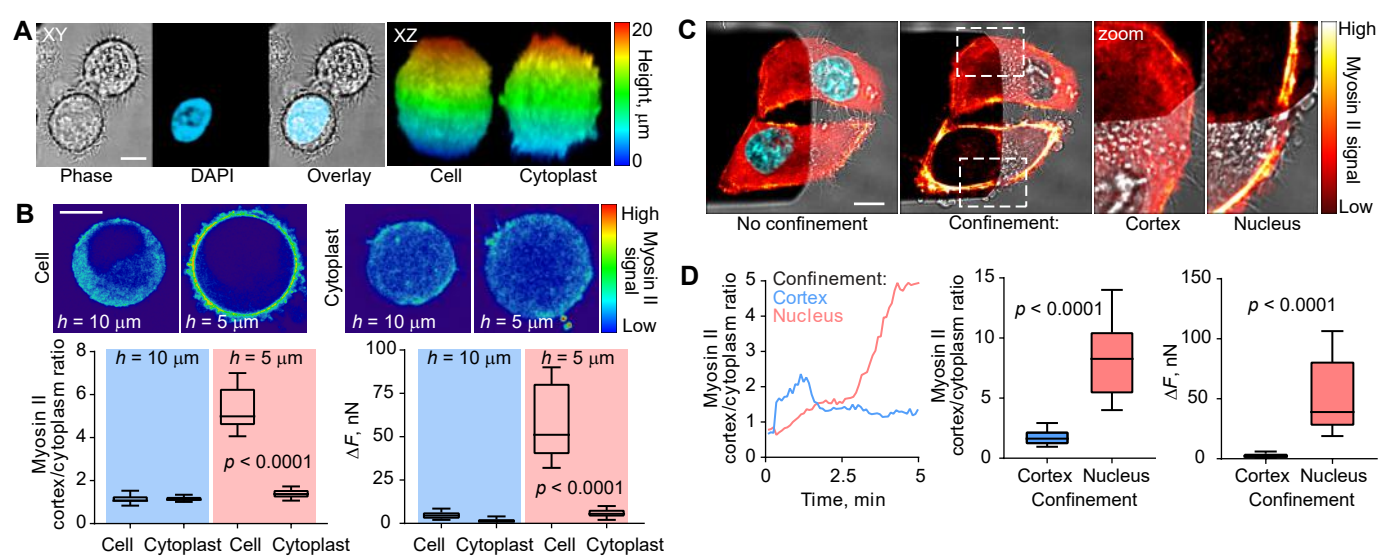
Movies S1-S7

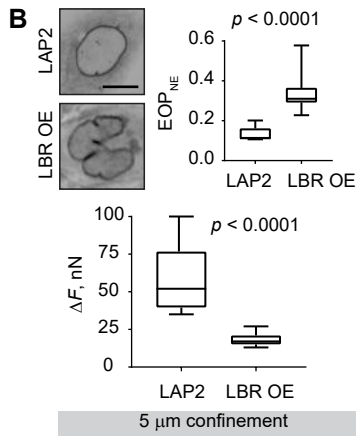
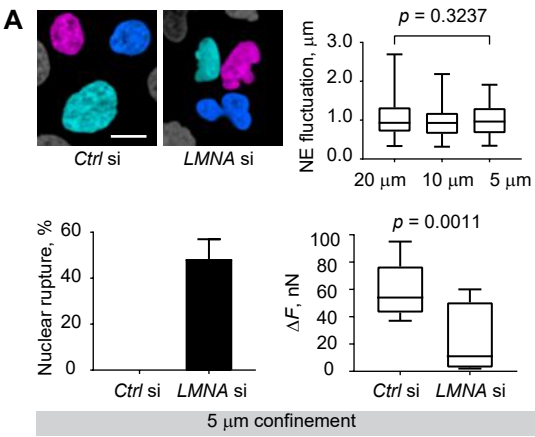


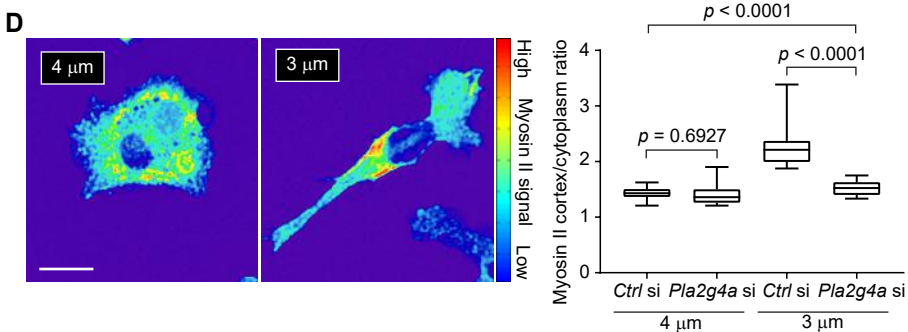
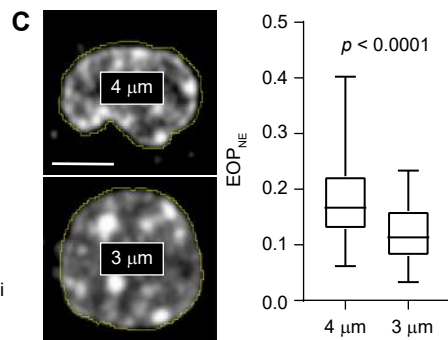
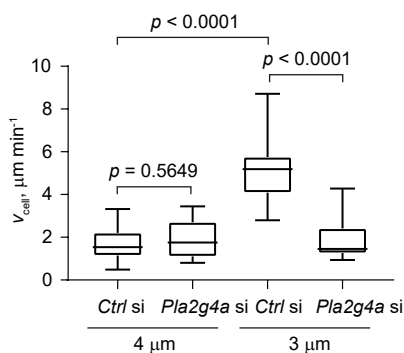
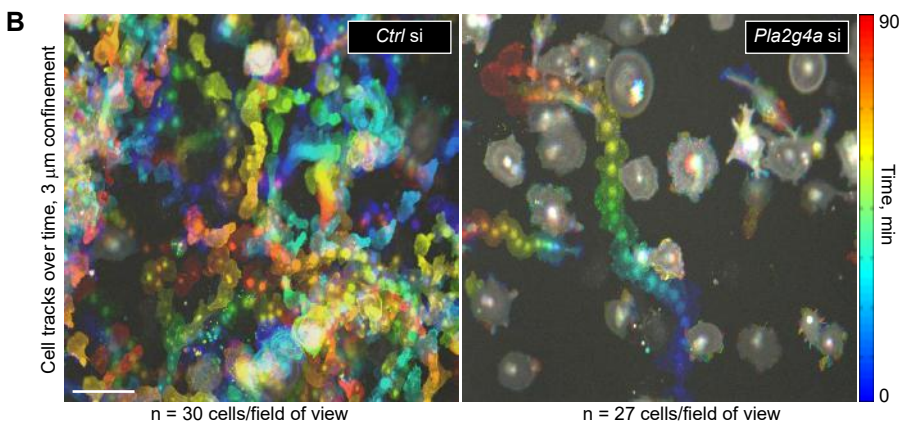
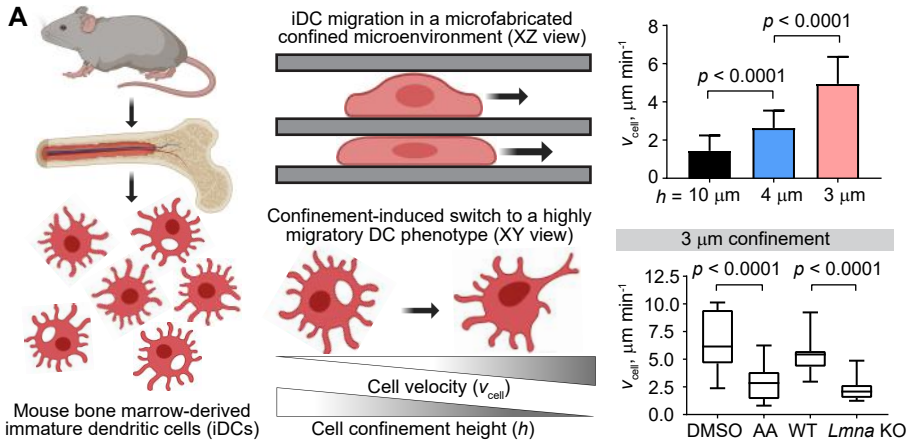


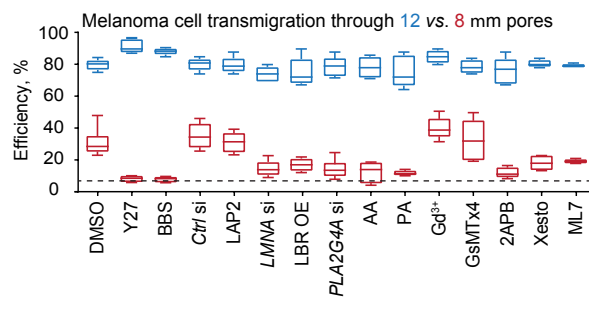
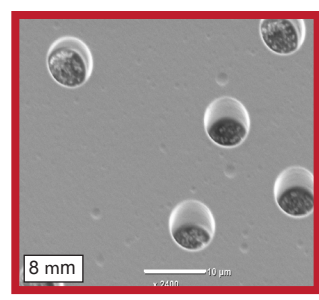
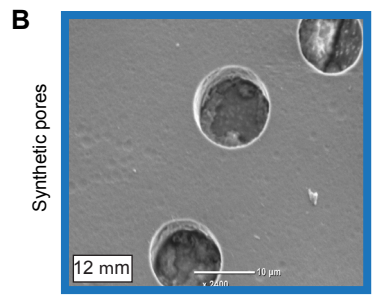
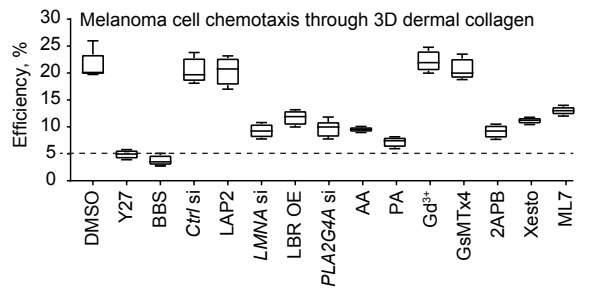
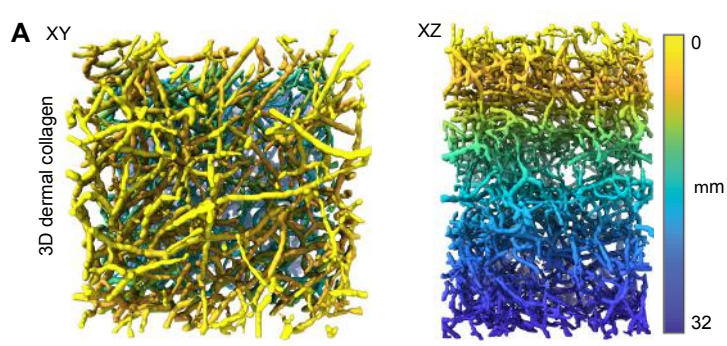












Supplementary Materials for

The nucleus acts as a ruler tailoring cell responses to spatial constraints

A.J. Lomakin, C.J. Cattin, D. Cuvelier, Z. Alraies, M. Molina, G.P.F. Nader, N. Srivastava, P.J. Saez, J.M. Garcia-Arcos, I.Y. Zhitnyak, A. Bhargava, M.K. Driscoll, E.S. Welf, R. Fiolka, R.J. Petrie, N.S. De Silva, J.M. González-Granado, N. Manel, A.M. Lennon-Duménil, D.J. Müller, M. Piel

Corresponding authors:

alexis.lomakin@ccri.at, daniel.mueller@bsse.ethz.ch, matthieu.piel@curie.fr.

This PDF file includes:

Figs. S1 to S11
Tables S1 to S3
Captions for Movies S1 to S7

Other Supplementary Materials for this manuscript include the following:

Movies S1 to S7

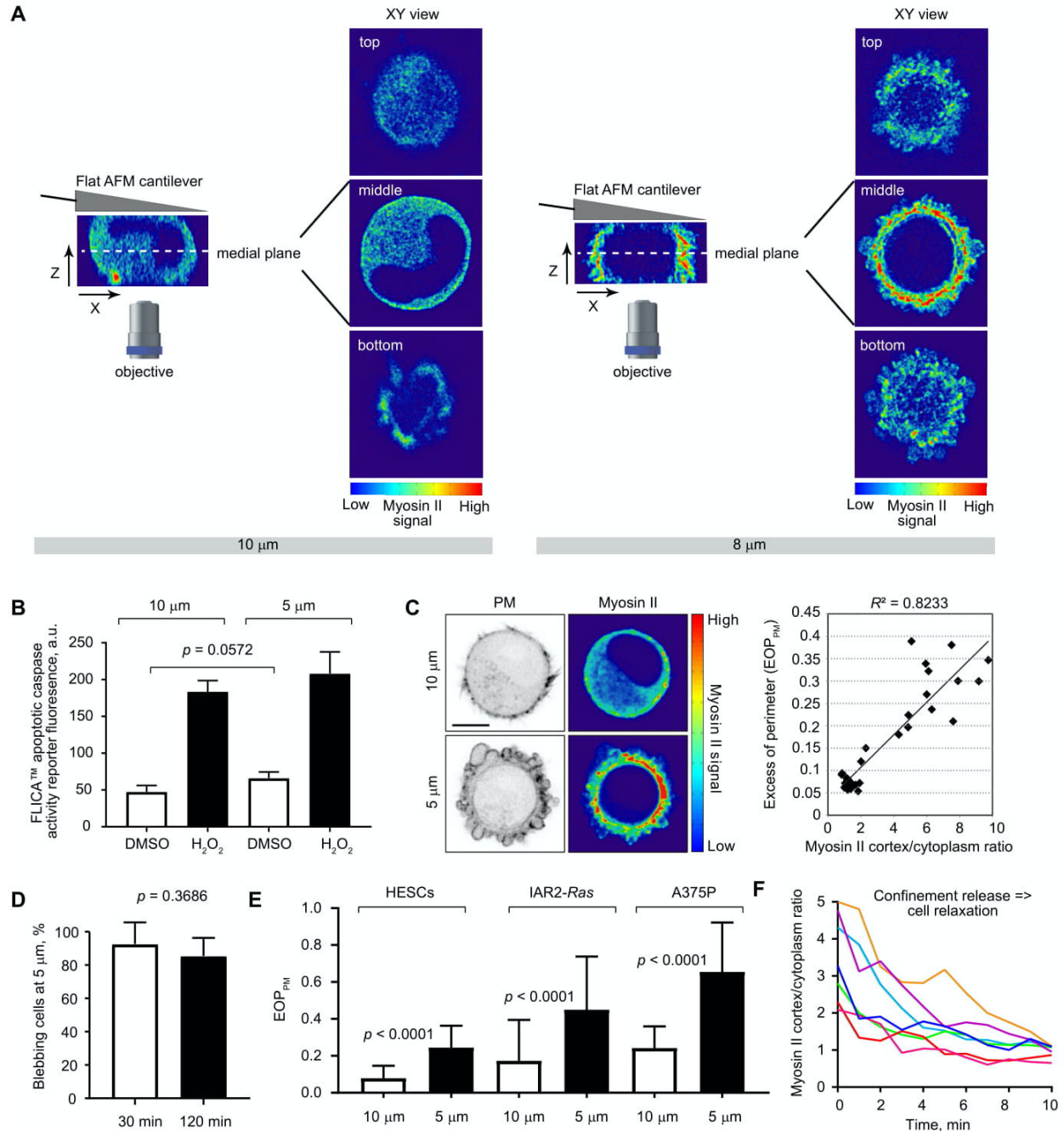


Fig. S1.

Experimental setup for quantification of the cortex-to-cytoplasm ratio of myosin II and plasma membrane blebbing upon cell confinement; Non-apoptotic plasma membrane blebbing associated with the contractile response to threshold confinement is sustained over time, observed in different cell types, and represents a reversible phenomenon.

A: Comparison of myosin II distribution in a representative example of a cell displaying the contractile force response (based on AFM output force registration paralleled with myosin II fluorescence imaging) at 8 μm confinement height. Note, the cell at 10 μm (left) has a diffused,

cytosolic distribution of myosin II signal, which is most evident upon examination of a medial plane of the cell on the XY projection. However, once the cell height is gradually ($10\ \mu\text{m} \rightarrow 9\ \mu\text{m} \rightarrow 8\ \mu\text{m}$) reduced to $8\ \mu\text{m}$ (right), myosin II re-localizes from the cytosol to the contractile cortex in this example. The XZ projection of the cell shows that this pattern is not unique to a single medial plane in XY coordinates. Myosin II displays a robust cortical accumulation across entire lateral parts of the cell but is less apparent in top and bottom parts of the cell cortex. This might be due to the fact that the plasma membrane is sterically restricted to bulge out at these sites, which interferes with the continuous blebbing required to maintain high cortical myosin II levels – contraction of the cortex enriched with myosin II induces pressure-based plasma membrane blebs which in turn accumulate myosin II at their own cortex; subsequent retraction of these blebs enables incorporation of the bleb-associated cortical myosin-II-F-actin into the main cortical actomyosin ring, further fueling the continuous cycle of global cortex contraction-local bleb formation-bleb retraction-cortex reformation. The example of a cell at $10\ \mu\text{m}$ vs. $8\ \mu\text{m}$ was chosen because the myosin II accumulation across entire lateral parts of the cells is visually clearer at this confinement height; cells demonstrating the contractile force response at heights lower than $8\ \mu\text{m}$ have the same myosin II distribution pattern.

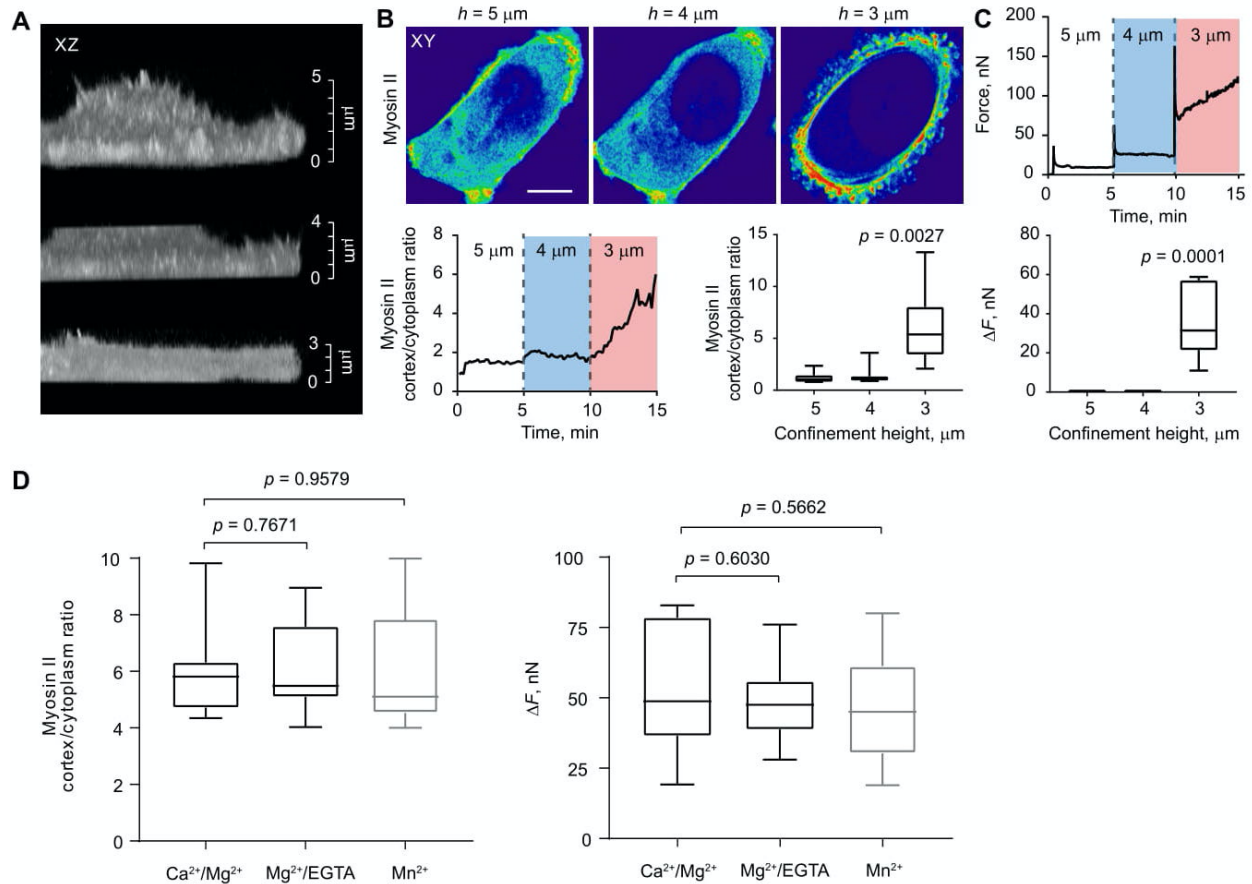
B: Comparing apoptosis induction efficiency (quantified as average fluorescence intensity of the FLICA apoptotic caspase activity reporter in cells) in response to spatial confinement of cells to 10 and $5\ \mu\text{m}$ vs. treatment of cells with a classical apoptosis inducer hydrogen peroxide (H_2O_2 , 1mM) as a positive control. Mean \pm SD; $n = 85$ cells from 3 independent fields of view per each experimental condition; p value, unpaired t test.

C: The plasma membrane (PM) blebbing index, measured as the excess of plasma membrane perimeter (EOP_{PM}), correlates with cortical accumulation of myosin II in cells under $5\ \mu\text{m}$ confinement ($n = 35$ cells). Scale bar, $10\ \mu\text{m}$.

D: Percentage of blebbing cells 30 and 120 minutes post $5\ \mu\text{m}$ -confinement. Mean \pm SD; $n = 120$ cells per each time point from 3 independent fields of view; p value, unpaired t test.

E: Quantifications of the plasma membrane (PM) blebbing index measured as the excess of plasma membrane perimeter (EOP_{PM}) at 10 and $5\ \mu\text{m}$ confinement in primary human epidermal stem cells (HESCs, $n = 45$ cells per each height), immortalized *N-ras*-transformed rat liver hepatocytes IAR-2 ($n = 150$ cells per each height), and human melanoma cell line A375P ($n = 40$ cells per each height). Mean \pm SD; p value, unpaired t test.

F: Quantifications of myosin at the cortex in response to release of spatial confinement ($n = 7$ cells).

**Fig. S2.**

Cells adhered to the substrate sense spatial confinement, but due to spreading-associated flattening respond to critical confinement at heights lower than those established for rounded nonadherent cells. Experimental modulation of integrin engagement during the contact of rounded nonadherent cells with the surface of the confining AFM cantilever does not change the contractile cell output upon confinement.

A: 3D images (XZ views) of the same single live HeLa-Kyoto spread cell expressing MYH9-GFP at 5, 4, and 3 μm confinement height.

B: Top, myosin II fluorescence intensity levels in the same single live cell (XY views) sequentially subjected to 5, 4, and 3 μm confinement. Bottom left, a representative graph illustrating dynamic relocalization of myosin II from the cytoplasm to the cell cortex in the same single live cell sequentially confined to 5, 4, and 3 μm . Bottom right, statistical analysis of cortical accumulation of myosin II detected in different cells at 5, 4, and 3 μm confinement. Mean \pm SD; $n = 7$ cells per each height; p value, unpaired t test. Scale bar, 10 μm .

C: Top, a representative force response curve of the same single live cell sequentially confined to 5, 4, and 3 μm . Bottom, statistical analysis of force response output (ΔF) detected in different cells at 5, 4, and 3 μm confinement. Mean \pm SD; $n = 10$ cells per each height; p value, unpaired t test.

D: Changing extracellular cations from $\text{Ca}^{2+}/\text{Mg}^{2+}$ to $\text{Mg}^{2+}/\text{EGTA}$ and to Mn^{2+} to allosterically switch integrins between low and high affinity conformations (ref. 11 in the main text) in rounded nonadherent cells does not significantly affect the fold increase in cortical myosin II accumulation

or contractile force production in response to 5 μm confinement. Mean \pm SD; $n = 10$ cells per each experimental condition; p value, unpaired t test.

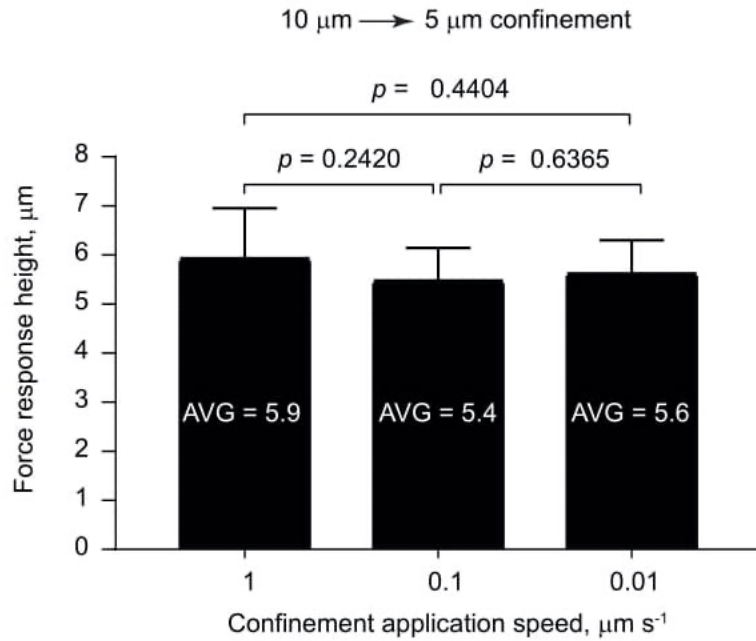


Fig. S3.

The height for contractile force response is insensitive to cell deformation rate.

Statistical analysis of the dependence between the confinement height at which cells display a robust contractile force response ($\Delta F > 15$ nN) to 10-to-5 μm confinement and the speed with which the confinement is applied. Mean \pm SD; $n = 10$ cells per each experimental condition; p value, unpaired t test.

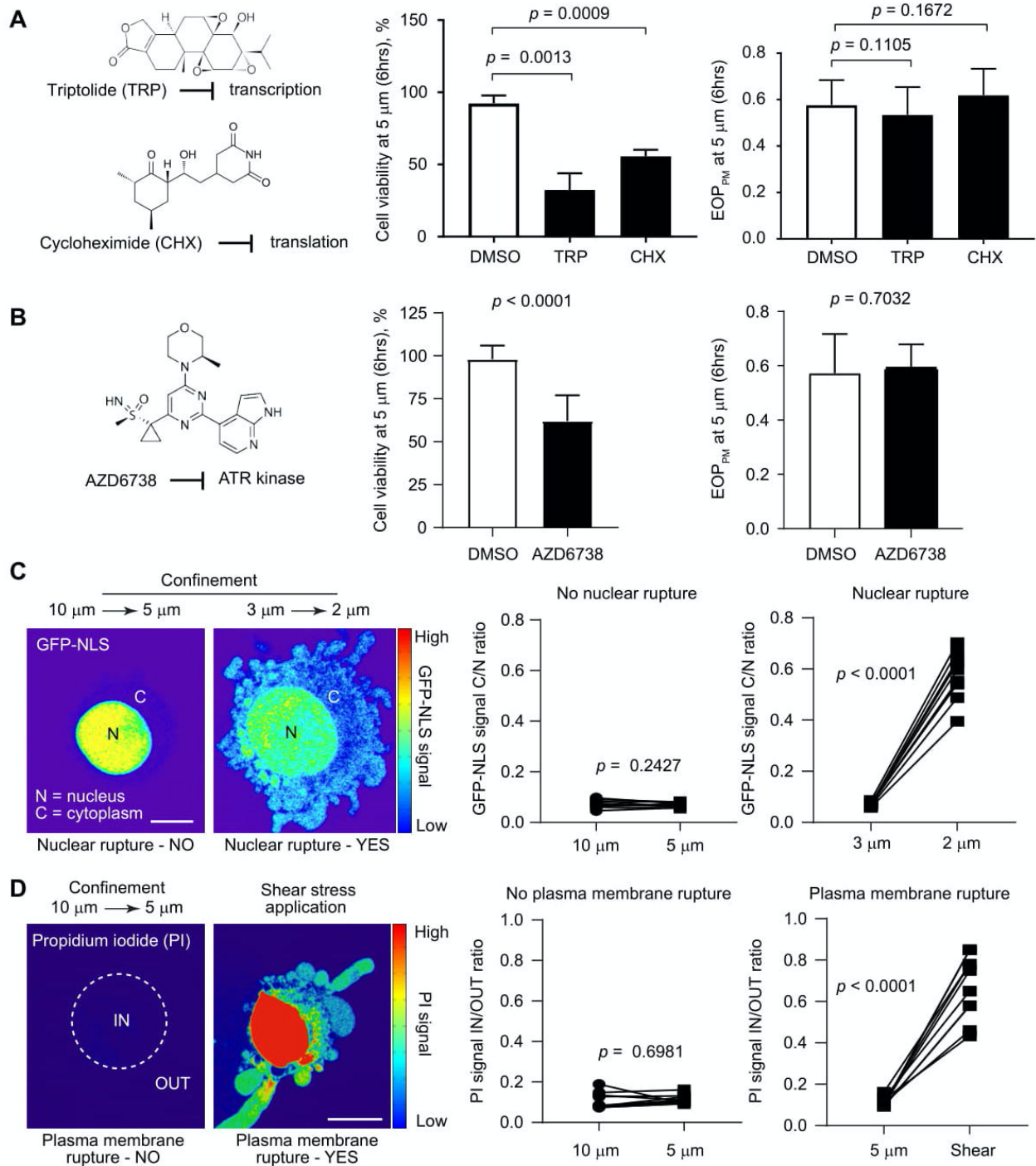


Fig. S4.

Testing alternative mechanisms potentially implicated in the activation of myosin II-based contractility in response to precise confinement.

A: Pretreatment of cells with pharmacological inhibitors of global transcription (Triptolide (TRP), 1 μM) and translation (Cycloheximide (CHX), 50 $\mu\text{g mL}^{-1}$) does not interfere with the contractile cell output in the form of plasma membrane blebbing measured as EOP_{PM} in cells under 5 μm

confinement (right, mean \pm SD; n = 35 cells per each experimental condition; *p* value, unpaired t test). The effect of the inhibitors on cell viability (middle) is used as a positive control for the inhibitors' activity (mean \pm SD; n = 150 cells per each experimental condition; *p* value, unpaired t test).

B: Pretreatment of cells with a pharmacological inhibitor (AZD6738, 1 μ M) of ATR kinase known to be sensitive to nuclear envelope tension (15) does not interfere with the contractile cell output in the form of plasma membrane blebbing measured as EOP_{PM} in cells under 5 μ m confinement (right, mean \pm SD; n = 40 cells per each experimental condition; *p* value, unpaired t test). The effect of the ATR kinase inhibitor on cell viability (middle) is used as a positive control for the inhibitor's activity (mean \pm SD; n = 150 cells per each experimental condition; *p* value, unpaired t test).

C: Representative images of a GFP-labeled nuclear localization sequence (NLS) probe in cells subjected to 10-to-5 μ m confinement (no nuclear rupture) vs. 3-to-2 μ m confinement (nuclear rupture = positive control). Appearance of the GFP-NLS signal in the cytoplasm is a sign of nuclear membrane rupture. Measurements of the GFP-NLS signal subcellular redistribution in the same living cell subjected to 10-to-5 μ m confinement (middle, n = 10 different cells; *p* value, paired t test) or 3-to-2 μ m confinement (right, n = 10 different cells; *p* value, paired t test) confirm that confining cells to 5 μ m height does not rupture the nuclear membrane. Scale bar, 10 μ m.

D: Representative images of Propidium iodide (PI) fluorescence in cells subjected to 10-to-5 μ m confinement (no plasma membrane rupture) vs. shear stress (plasma membrane rupture = positive control). PI can enter the cell through nonspecific pores/wounds in the plasma membrane and becomes fluorescent after binding to cytoplasmic RNA or nuclear DNA molecules. Measurements of PI fluorescence levels in the same living cell subjected to 10-to-5 μ m confinement (middle, n = 10 different cells; *p* value, paired t test) or shear stress (right, n = 10 different cells; *p* value, paired t test), confirm that cell confinement *per se* does not rupture the plasma membrane. Scale bar, 15 μ m.

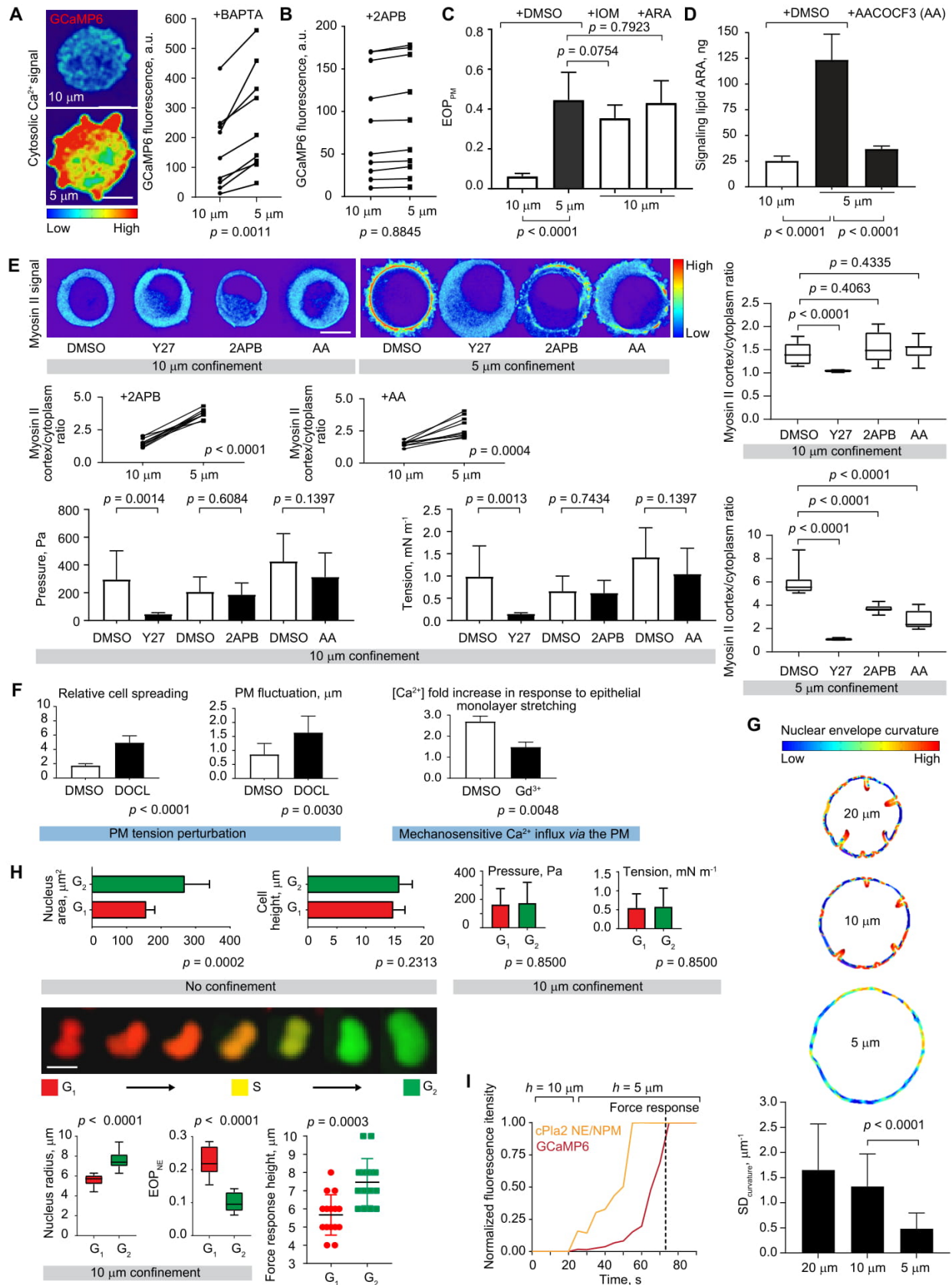


Fig. S5.**Molecular pathways associated with nuclear and perinuclear ER membrane stretch become engaged at 5 μm confinement height without affecting cell behaviors at 10 μm height.**

A: Left, representative images illustrating that intracellular Ca^{2+} concentration increases in response to 10-to-5 μm confinement even in the presence of 2 mM BAPTA chelating extracellular Ca^{2+} . Right, measurements of cytoplasmic fluorescence intensity for the genetically encoded fluorescence Ca^{2+} sensor GCaMP6 in the same living cell subjected to 10-to-5 μm confinement in the presence of 2 mM BAPTA ($n = 10$ different cells; p value, paired t test). Scale bar, 10 μm .

B: Measurements of GCaMP6 fluorescence levels in the same BAPTA (2 mM)-treated living cell subjected to 10-to-5 μm confinement in the presence of 100 μM 2APB inhibiting the stretch sensitive Ca^{2+} -channels InsP3R present on the perinuclear ER and nuclear membranes ($n = 10$ different cells; p value, paired t test).

C: Comparing the contractile cell output in the form of plasma membrane blebbing measured as EOP_{PM} in cells under different degrees of spatial confinement in the presence of 1% DMSO (control), 10 μM ionomycin (IOM, artificially increasing the intracellular Ca^{2+} level), or 70 μM arachidonic acid (ARA, the signaling lipid-product of enzymatic activity of the nuclear membrane stretch-sensitive protein cPLA2). Mean \pm SD; $n = 35$ cells per each experimental condition; p value, unpaired t test.

D: Biochemical measurements of ARA release in cell populations confined to 10 or 5 μm in the presence or absence of a cPLA2 inhibitor AACOCF3 (AA, 20 μM ; $n = 3$ replicates; mean \pm SD; p value, unpaired t test).

E: Top, representative single medial confocal slice images of myosin II fluorescence in cells at 10 vs. 5 μm confinement in the presence of 1% DMSO (control) or the drugs Y27 (Y27632, 10 μM (global downregulation of myosin II activity)), 2APB (100 μM (blockage of the stretch-sensitive Ca^{2+} -channels InsP3R on nuclear and perinuclear ER membranes)), and AA (AACOCF3, 20 μM (inhibition of the nuclear membrane stretch-sensitive protein cPLA2)). Scale bar, 10 μm .

Middle, change in myosin II cortex/cytoplasm ratio measured in the same single live cell confined to 10 μm and subsequently 5 μm in the presence 100 μM 2APB or 20 μM AA. The measurements were done 5 minutes after application of each confinement height ($n = 10$ different cells per each experimental condition; p value, paired t test). The two (upper and lower) graphs on the right side of the panel demonstrate statistical analyses of myosin II cortex/cytoplasm ratio at 10 and 5 μm confinement in cells treated with 1% DMSO or the drugs Y27 (10 μM), 2APB (100 μM), and AA (20 μM). Mean \pm SD; $n = 30$ cells per each experimental condition; p value, unpaired t test. The measurements were done 5 minutes after application of the specified confinement height. Unlike perturbations that impact basal levels of actomyosin contractility (e.g. Y27, which entirely prevents cells from accumulating myosin II at the cortex in response to 10-to-5 μm -confinement, as shown in Fig. 1D), the drugs affecting the nuclear ruler pathway (2APB and AA) do not prevent cells from accumulating myosin II at the cortex in response to 10-to-5 μm -confinement. Such cells do change their myosin II cortex/cytoplasmic ratio in a statistically significant manner, but the fold change is statistically smaller than in control cells (see additionally Fig. 1D). These data suggest that the drugs are unlikely to affect the actomyosin cytoskeleton prior to the 5 μm confinement step. Indeed, as follows from the upper right graph here, Y27 cancels the small variations in the cortex/cytoplasm ratio of myosin II at 10 μm ; while the drugs affecting the nuclear ruler pathway have no statistically significant impact on the myosin II cortex/cytoplasm ratio at 10 μm .

Bottom, biophysical measurements of cell mechanics at 10 μm confinement height. Unlike perturbations that impact basal levels of actomyosin contractility (e.g. Y27, 10 μM), 100 μM 2APB

and 20 μM AA do not change intracellular pressure and cortical tension estimated in cells at 10 μm confinement. Mean \pm SD; $n = 10$ cells per each experimental condition; p value, unpaired t test.

F: Left, measurements demonstrating that 0.4 mM deoxycholate (DOCL) does perturb plasma membrane (PM) tension as evidenced from DOCL's effect on relative cell spreading and fast fluctuations of the plasma membrane ($n = 10$ cells per each measurement; mean \pm SD; p value, unpaired t test). Right, measurements of Ca^{2+} entry into the cell upon stretching MDCK cell monolayers grown on flexible PDMS membranes in the presence or absence of 10 μM GdCl_3 inhibiting stretch-sensitive ion channels on the plasma membrane ($n = 3$ replicates; mean \pm SD; p value, unpaired t test).

G: Automatic curvature detection in representative single, medial confocal slice images of the nuclear envelope in control HeLa-Kyoto cells expressing LAP2-GFP (a marker of the nuclear envelope). The images illustrate that nuclear envelope curvature decreases in the same living cell subjected to 20-to-10-to-5 μm confinement. The graph below demonstrates statistical analysis of standard deviation of nuclear envelope curvature ($\text{SD}_{\text{curvature}}$) in cells at 20 μm ($n = 16$ cells), 10 μm ($n = 19$ cells), and 5 μm ($n = 15$ cells). Mean \pm SD; p value, unpaired t test.

H: Upper left, quantifications of nuclear size and cell height illustrating that rounded nonadherent G_1 ($n = 10$) and G_2 ($n = 10$) cells have a similar height, but different nuclear size at resting state (no confinement). Upper right, quantifications of intracellular pressure and cortical tension in G_1 ($n = 10$) vs. G_2 ($n = 10$) cells illustrating that the cell cycle stage *per se* does not affect basal levels of actomyosin contractility that controls cortical cell tension and intracellular pressure at 10 μm confinement. Lower middle, naturally occurring dynamic changes in nuclear shape and size accompanying cell cycle progression in the same live HeLa-Kyoto cell expressing the FUCCI fluorescent cell cycle reporter system. Lower bottom, quantifications revealing differences in nuclear size (radius) and folding (EOP_{NE}) in G_1 ($n = 10$) vs. G_2 ($n = 10$) cells under 10 μm confinement, and differential height-dependence of contractile force response in G_1 ($n = 15$) vs. G_2 ($n = 15$) cells. Mean \pm SD; p value, unpaired t test. Scale bar, 10 μm .

I: A representative graph illustrating that an increase in cytosolic Ca^{2+} and the accumulation at the nuclear envelope of the nuclear envelope stretch-sensitive enzyme cPlA2-mKate2 temporally precede contractile force response measured with the flat AFM microcantilever. This phenomenon is observed in almost 100% of analyzed cases ($n = 30$ cells).

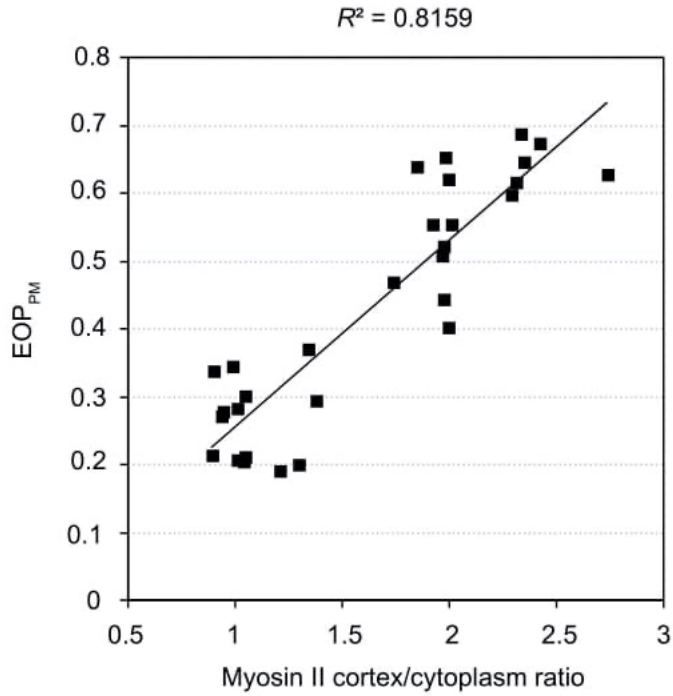


Fig. S6.

Interdependence between the degree of plasma membrane blebbing and myosin II accumulation at the cortex in human fibrosarcoma cells maneuvering through 3D cell derived matrices.

Correlation between the cell blebbing index measured as the excess of plasma membrane perimeter and cortical accumulation of myosin II in HT1080 cells imaged within the 3D dermal fibroblast-derived cell matrix (n = 30 cells).

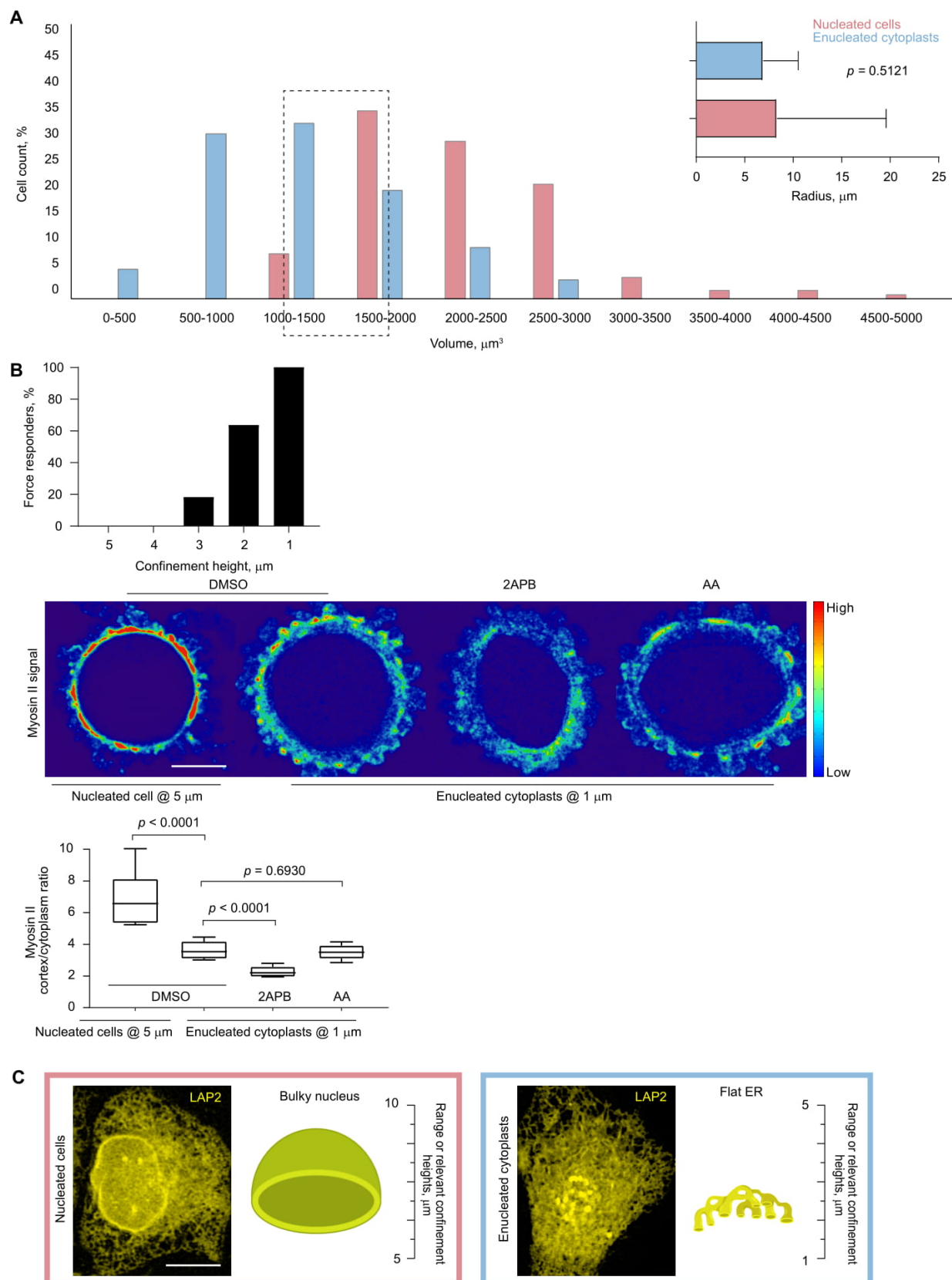


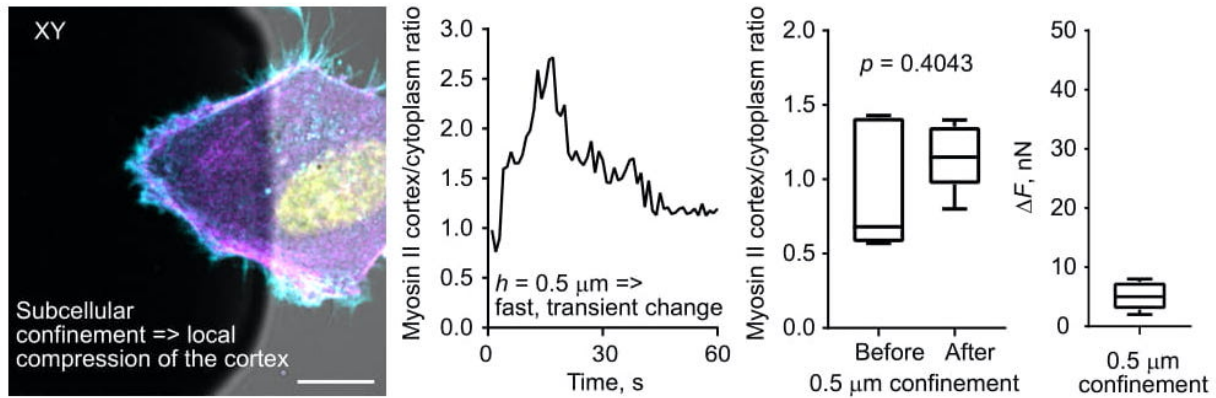
Fig. S7.

Rounded enucleated cytoplasts possess a wide range of sizes, and those matching nucleated cell sizes are still incapable of measuring confinement height within the range of 10 to 5 μm .

A: Large-scale statistical analysis of enucleated cytoplast size ($n = 150$) vs. nucleated cell size ($n = 100$, p value, unpaired t test).

B: Top, unlike rounded nucleated cells upon centrifugation, rounded enucleated cytoplasts with a similar size ($\sim 15 \mu\text{m}$ in diameter) do not respond to 10-to-5 μm confinement and begin measuring confinement height at significantly lower heights with a strong preference to 1 μm confinement ($n = 25$ cytoplasts with diameter $\geq 15 \mu\text{m}$). Middle and bottom, representative single medial confocal slice images of myosin II fluorescence as well as statistical analysis of myosin II cortex/cytoplasm ratio demonstrate that similar to nucleated cells at 5 μm , enucleated cytoplasts at 1 μm also increase myosin II concentration at the cortex (see Fig. 5D for myosin II cortex/cytoplasm ratio in enucleated cytoplasts at 5 μm); however, the fold increase is statistically smaller than in nucleated cells, indicating that there is no complete activation of myosin II in enucleated cytoplasts. 100 μM 2APB blocking intracellular calcium release from internal membrane storages (e.g. ER membranes), but not 20 μM AA (AACOCF3) inhibiting nuclear cPLA2, leads to a statistically significant decrease in myosin II cortex/cytoplasm ratio in enucleated cytoplasts at 1 μm . Mean \pm SD; $n = 10$ per each experimental condition; p value, unpaired t test.

C: Representative images of LAP2-GFP subcellular distribution illustrating that both nucleated cells and enucleated cytoplasts preserve an elaborate system of ER membranes that could take over the ruler function of the nucleus at significantly lower confinement heights. Scale bar, 10 μm .

**Fig. S8.****Cortex compression in the lamellar region of the cell devoid of bulky cytoplasmic organelles.**

Left, an image illustrating the position of the flat microcantilever to achieve a local compression of the cortex in the lamellar region of the cell (cyan, F-actin; magenta, myosin II; yellow, nucleus; scale bar, 10 μm), and quantification of the fast and transient increase in cortical myosin II signal upon strong (0.5 μm height confinement) compression of the cell cortex (the rapid and transient nature of the myosin II signal increase followed by decline to the initial level in response to local 0.5 μm compression of the lamellar region was observed in almost 100 % of analyzed cells ($n = 15$)). Right, statistical analyses of cortical accumulation of myosin II before and 5 minutes after 0.5 μm confinement of the cortex and force readouts after 0.5 μm confinement of the cortex ($n = 10$ cells; mean \pm SD; p value, unpaired t test).

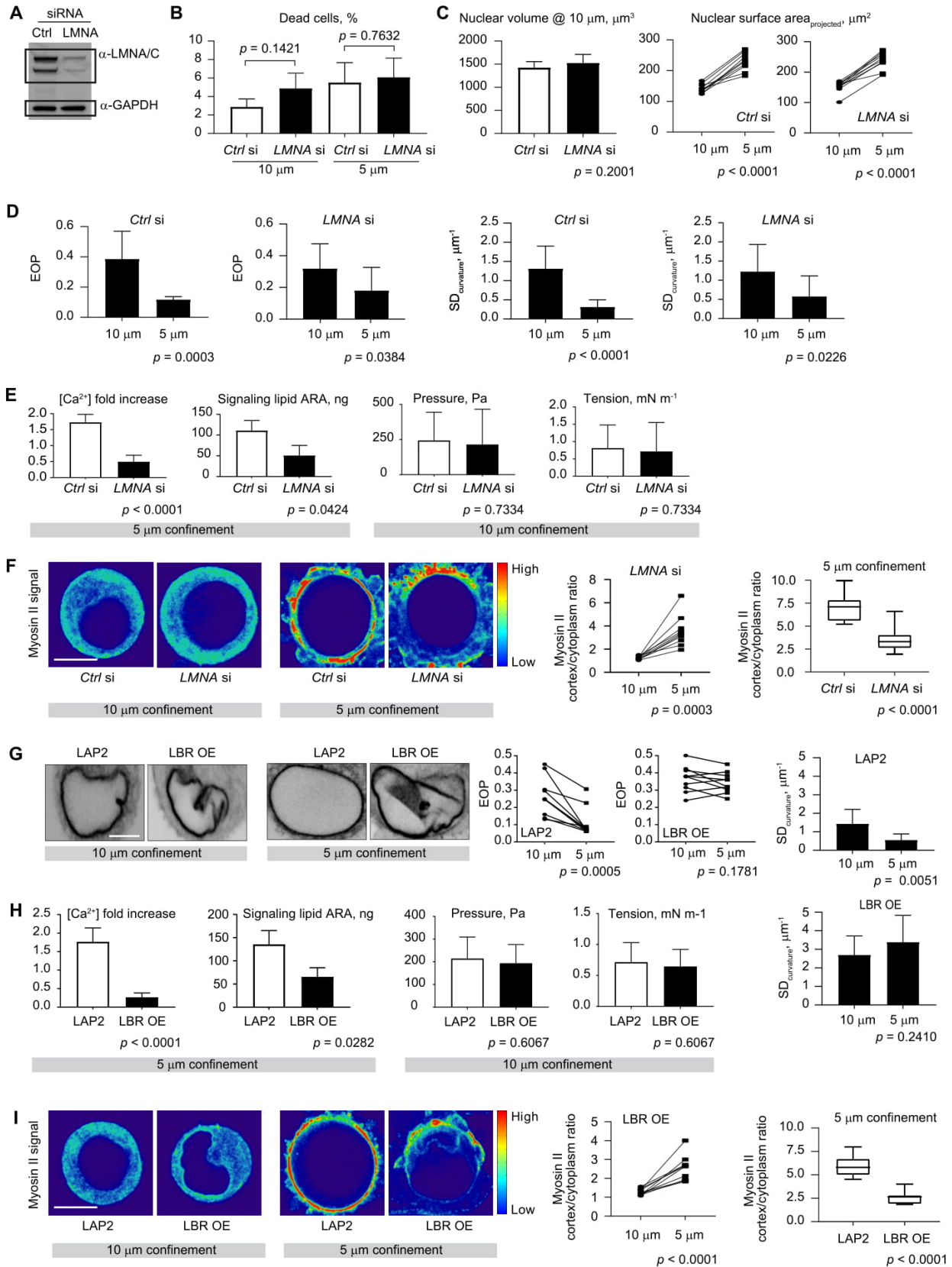


Fig. S9.

Experimental perturbations targeting the ruler function of the nucleus do not affect basal contractility levels at 10 μm height, but significantly impact the signaling upstream of actomyosin activity at 5 μm confinement height.

A: Nuclear LMNA knockdown efficiency in HeLa-Kyoto cells revealed with Western blotting.

B: Percentage of propidium iodide (PI)-positive (dead) control (*Ctrl* si) and LMNA-depleted (*LMNA* si) cells upon confinement to 10 and 5 μm . Mean \pm SD; data are from 3 replicates; $n = 200$ cells per each experimental replicate; p value, unpaired t test.

C: Left, nuclear volume measurements in control (*Ctrl* si) and LMNA-depleted (*LMNA* si) cells at 10 μm confinement. Mean \pm SD; $n = 30$ cells per experimental condition; p value, unpaired t test. Right, measurements of projected nuclear surface area taken for the nucleus from the same single live cell at 10 vs. 5 μm in control (*Ctrl* si) and LMNA-depleted (*LMNA* si) cells ($n = 10$ different cells; p value, paired t test).

D: Quantifications illustrating the degree of nuclear envelope folding (measured as excess of perimeter of the nuclear envelope (EOP_{NE}) or standard deviation of nuclear envelope curvature ($\text{SD}_{\text{curvature}}$)) in control (*Ctrl* si) and LMNA-depleted (*LMNA* si) cells upon confinement to 10 and 5 μm . Mean \pm SD; $n = 30$ cells per each experimental condition, p value, unpaired t test.

E: Left, quantifications illustrating the effect of nuclear LMNA knockdown on the increase of intracellular Ca^{2+} concentration and production of the signaling lipid ARA in response to 5 μm confinement ($n = 3$ replicates per each experimental condition; mean \pm SD; p value, unpaired t test). Right, quantifications of intracellular pressure and cortical tension in control ($n = 10$) vs. LMNA depleted ($n = 10$) cells illustrating that LMNA depletion does not affect basal levels of actomyosin contractility that controls cortical cell tension and intracellular pressure at 10 μm confinement. Mean \pm SD; p value, unpaired t test.

F: Left, representative single medial confocal slice images of myosin II fluorescence in control (*Ctrl* si) and LMNA-depleted (*LMNA* si) cells. Scale bar, 10 μm . Middle, measurements of myosin II cortex/cytoplasm ratio obtained from the same single live cell confined to 10 μm and subsequently 5 μm . The measurements were done 5 minutes after application of each confinement height ($n = 10$ different cells per each experimental condition; p value, paired t test). Right, statistical analysis of myosin II cortex/cytoplasm ratio at 5 μm confinement. Mean \pm SD; $n = 30$ cells per each experimental condition; p value, unpaired t test. The measurements were done 5 minutes after application of the specified confinement height. LMNA depleted cells do change their myosin II cortex/cytoplasmic ratio in a statistically significant manner, but the fold change is significantly smaller than in control cells (see additionally Fig. 1D).

G: Representative images of nuclei in control LAP2-GFP expressing cells and LBR-GFP overexpressing (OE) cells at 10 vs. 5 μm confinement (scale bar, 5 μm) and quantifications of the degree of nuclear envelope folding measured as excess of perimeter of the nuclear envelope (EOP_{NE}) in the same single live cell upon 10-to-5 μm confinement in LAP2-GFP expressing cells and LBR-GFP OE cells ($n = 10$ different cells per each experimental condition; p value, paired t test). Measurements of standard deviation of nuclear envelope curvature ($\text{SD}_{\text{curvature}}$) in LAP2-GFP expressing cells and LBR-GFP OE cells at 10 and 5 μm confinement are shown on the right top and bottom graphs. Mean \pm SD; $n = 20$ cells per each experimental condition; p value, unpaired t test.

H: Left, quantifications illustrating the effect of LBR-GFP OE on the increase of intracellular Ca^{2+} concentration and production of the signaling lipid ARA in response to 5 μm confinement ($n = 3$ replicates per each experimental condition; mean \pm SD; p value, unpaired t test). Right,

quantifications of intracellular pressure and cortical tension in control LAP2-GFP expressing cells ($n = 10$) vs. LBR-GFP OE cells ($n = 10$) illustrating that LBR-GFP OE does not affect basal levels of actomyosin contractility that controls cortical cell tension and intracellular pressure at $10\ \mu\text{m}$ confinement. Mean \pm SD; p value, unpaired t test. Scale bar, $10\ \mu\text{m}$.

I: Left, representative single medial confocal slice images of myosin II fluorescence in control LAP2-GFP expressing cells and LBR-GFP OE cells. Scale bar, $10\ \mu\text{m}$. Middle, measurements of myosin II cortex/cytoplasm ratio obtained from the same single live cell confined to $10\ \mu\text{m}$ and subsequently $5\ \mu\text{m}$. The measurements were done 5 minutes after application of each confinement height ($n = 10$ different cells per each experimental condition; p value, paired t test). Right, statistical analysis of myosin II cortex/cytoplasm ratio at $5\ \mu\text{m}$ confinement. Mean \pm SD; $n = 30$ cells per each experimental condition; p value, unpaired t test. The measurements were done 5 minutes after application of the specified confinement height. LBR-GFP OE cells do change their myosin II cortex/cytoplasmic ratio in a statistically significant manner, but the fold change is significantly smaller than in control cells (see additionally Fig. 1D).

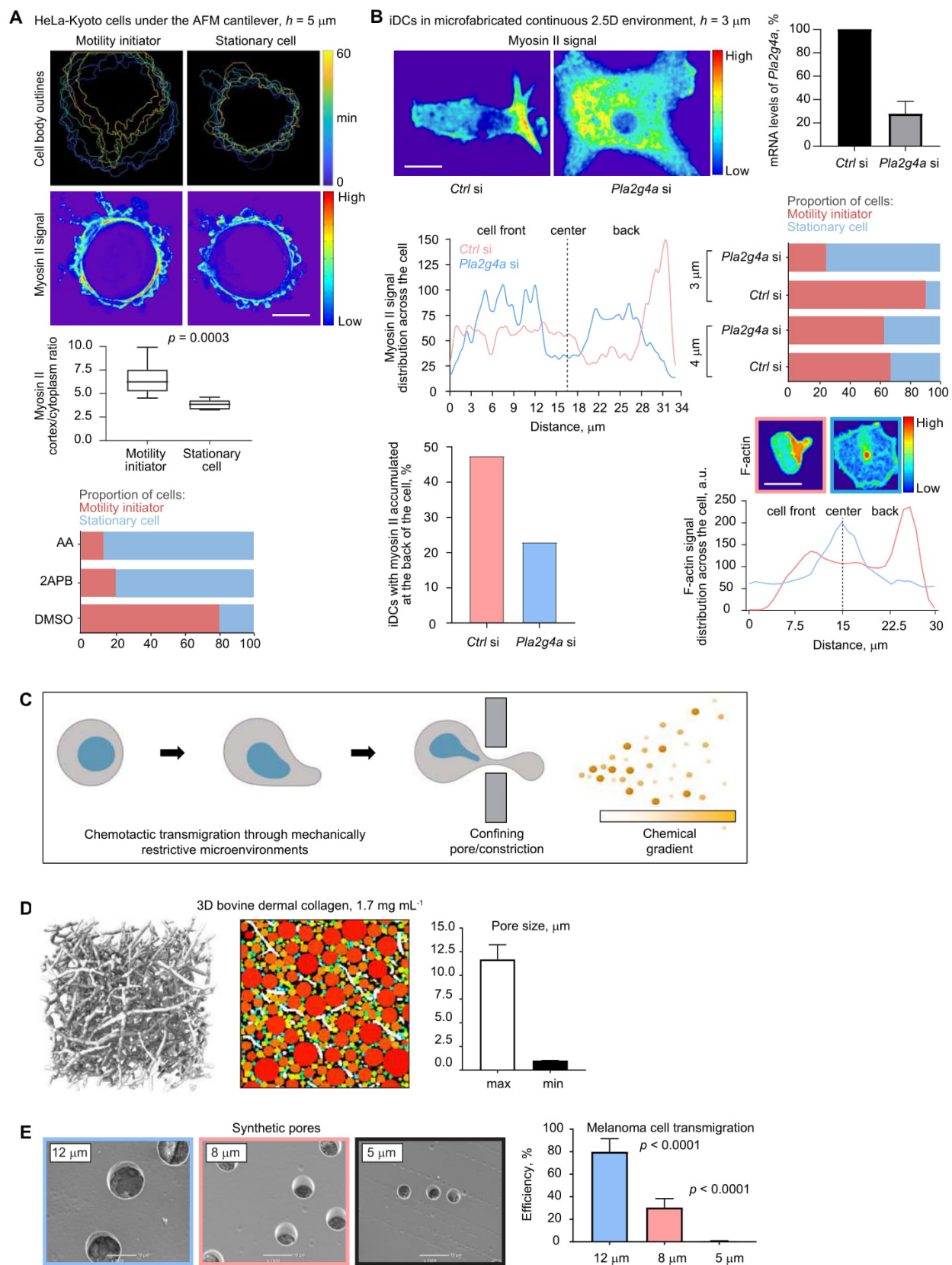


Fig. S10.**Testing the role of the nuclear ruler pathway in the process of cell migration in complex microenvironments.**

A: Top, representative images of HeLa-Kyoto cells kept under the confining AFM microcantilever for a prolonged period of time (1 hour). Cell body outlines were captured at different time points after application of 5 μm -confinement, differentially color-coded, and superimposed to reveal cell body movement over the entire observation period. Prolonged spatial confinement under the AFM microcantilever stimulates cell motility initiation – cells try to evade the microcantilever. Middle, single (midplane confocal slice) myosin II fluorescence images of the cell outlines depicted in the top panel above. Myosin II images were acquired 5 min after application of 5 μm confinement. Statistical analysis demonstrates that the fraction of cells remaining stationary under the confinement is characterized by a significantly lower ratio between cortical and cytosolic myosin II. Mean \pm SD; $n = 24$ cells (motility initiators) and 6 cells (stationary cells); p value, unpaired t test. Scale bar, 5 μm . Bottom, proportion of cells remaining stationary or initiating motility under the prolonged confinement in the absence (DMSO control) or presence of small-molecule compounds targeting proteins involved in the nuclear ruler pathway (20 μM AACOCF3 (AA) and 100 μM 2APB); $n = 30$ cells per each experimental condition.

B: Top left, representative images (maximum intensity projections) of Myh9-GFP-expressing control (*Ctrl* si) and cPLA2a-depleted (*Pla2g4a* si) mouse iDCs at 3 μm height. Top right, levels of depletion of cPLA2a (the *Pla2g4a* gene) in mouse iDCs. mRNA levels of cPLA2a quantified with qRT-PCR 72h after siRNA transfection. Values are normalized to mRNA levels of cPLA2a in control samples. Mean \pm SD; $n = 3$. Middle left, a representative line scan graph (obtained from maximum intensity projections images) demonstrating accumulation of myosin II fluorescence signal at the back of a typical iDC (*Ctrl* si) under 3 μm -confinement and a rather homogeneous front-back distribution of myosin II fluorescence in a typical cPLA2a-depleted iDC (*Pla2g4a* si) under 3 μm -confinement. Middle right, proportion of control (*Ctrl* si) and cPLA2a-depleted (*Pla2g4a* si) iDCs remaining stationary or initiating motility under prolonged (1.5 hr) 4 vs. 3 μm -confinement. cPLA2a functions become critical at stronger, 3 μm confinement, when the cell microenvironment is mechanically resistive to cell migration. $n = 60$ cells per each experimental condition. Bottom left, percentage of cells with myosin II accumulated at the back in control (*Ctrl* si) or cPLA2a-depleted (*Pla2g4a* si) iDCs under 3 μm confinement. $n = 60$ cells per each experimental condition. Bottom right, representative maximum intensity projection images of LifeAct-GFP-expressing motile (framed in pink) and stationary (framed in blue) iDCs under 3 μm confinement; the corresponding line scan graph demonstrates that F-actin fluorescence signal is characteristically accumulated at the back of the cell in motile iDCs (pink curve), while stationary iDCs (blue curve) show F-actin collapsed in the cell center. Scale bar, 30 μm .

C: A simplified cartoon illustrating cell and nuclear squeezing through a confining opening in the extracellular environment in response to a gradient of chemotactic molecules, the situation that can be modelled experimentally using the Boyden chamber transwell assay.

D: A representative 3D light sheet microscopy image of the dermal collagen lattice and an example of computer vision-aided pore size analysis by filling 3D spheres in between the collagen fibers in the skeletonized 3D image of the collagen lattice. The measurements show that the 3D collagen lattices represent an environment with pore sizes ranging from ~ 1 μm (minimum size) to 10 μm (maximum size) in diameter (graph shows measure for different lattices).

E: Scanning electron microscopy images of polycarbonate membranes with 12, 8, and 5 μm pores in diameter, and quantification of the percentage of human melanoma cells A375P able to

chemotactically transmigrate through the differentially-sized pores. The analysis shows that 5 μm pores are impenetrable for melanoma cells, 12 μm pores do not restrict cell migration, while 8 μm pores are rate-limiting to cell migration and thus ideally suited for the study of cell transmigration through mechanically restrictive environments. Mean \pm SD; data are from 3 replicates; $n = 200$ cells per each experimental replicate; p value, unpaired t test.

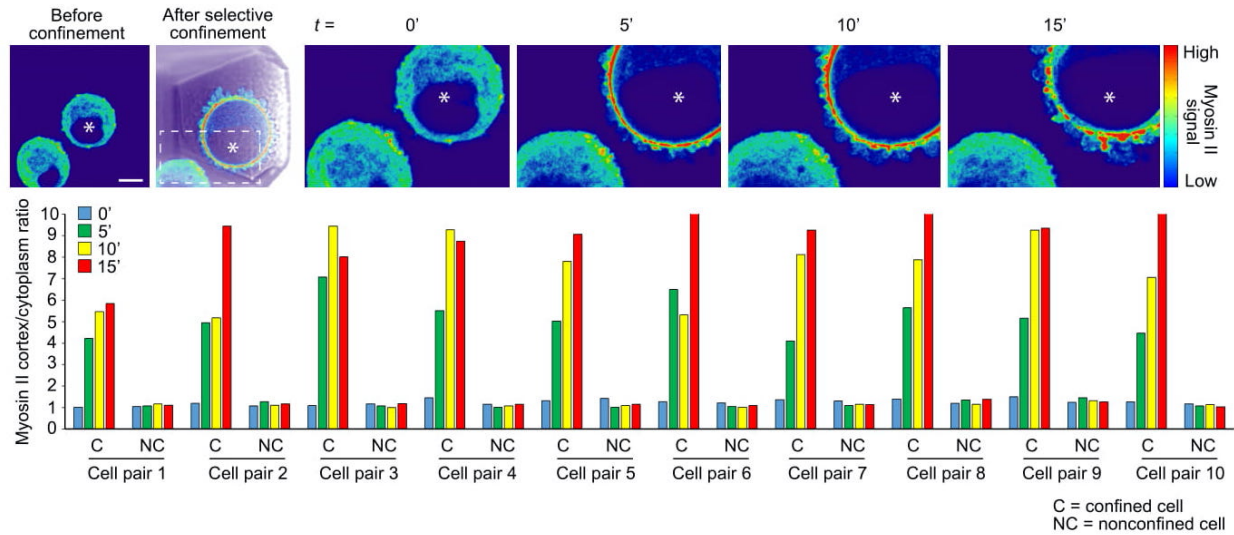


Fig. S11. Testing for a potential paracrine effect of contractility activation upon cell/nuclear compression. Selective, single-cell confinement of cell doublets, in which the distance between the plasma membrane of the adjacent cells is $\leq 3 \mu\text{m}$. $t = 0'$ corresponds to a state before confinement application; $t = 5'$ denotes conditions 5 minutes after selective application of $5 \mu\text{m}$ -height confinement; the selectively confined cell is marked with a star sign (*). Note, at least on the timescale of 15 minutes, the ratio between cortical and cytosolic myosin II is not changing in nonconfined cells (NC) compared to their immediate neighbors under confinement (C). In some cases, a local bias in cortical accumulation of myosin II between closely located cells was observed before confinement, however, this biased pattern was unstable after confinement application. Scale bar, $10 \mu\text{m}$.

Table S1. Description of chemicals used in the mini-screen

| Pharmacological perturbations affecting plasma membrane (PM) tension & extracellular Ca ²⁺ influx | | | Pharmacological perturbations affecting stretch-sensitive proteins of the nuclear envelope (NE)/perinuclear ER & intracellular Ca ²⁺ homeostasis | | |
|--|--|---|---|---|---|
| Drug name | Drug target/effect | Reference papers | Drug name | Drug target/effect | Reference papers |
| Deoxycholate (DOCL) | Reduces PM tension | <p>Raucher D, Sheetz MP. Cell spreading and lamellipodial extension rate is regulated by membrane tension. <i>J Cell Biol.</i> 2000 Jan 10;148(1):127-36.</p> <p>Raucher D, Sheetz MP. Membrane expansion increases endocytosis rate during mitosis. <i>J Cell Biol.</i> 1999 Feb 8;144(3):497-506.</p> | AACOCF3 (AA)/ PACOCF3 (PA) | Inhibits Ca ²⁺ -dependent, NE tension-sensitive enzyme cPLA ₂ producing the signaling lipid arachidonic acid (ARA) known to activate actomyosin contractility | <p>Ackermann EJ, Conde-Frieboes K, Dennis EA. Inhibition of macrophage Ca(2+)-independent phospholipase A2 by bromoenol lactone and trifluoromethyl ketones. <i>J Biol Chem.</i> 1995 Jan 6;270(1):445-50.</p> <p>Enyedi B, Jelcic M, Niethammer P. The Cell Nucleus Serves as a Mechanotransducer of Tissue Damage-Induced Inflammation. <i>Cell.</i> 2016 May 19;165(5):1160-1170.</p> <p>Peters-Golden M, Song K, Marshall T, Brock T. Translocation of cytosolic phospholipase A2 to the nuclear envelope elicits topographically localized phospholipid hydrolysis. <i>Biochem J.</i> 1996 Sep 15;318 (Pt 3):797-803.</p> <p>Schievella AR, Regier MK, Smith WL, Lin LL. Calcium-mediated translocation of cytosolic phospholipase A2 to the nuclear envelope and endoplasmic reticulum. <i>J Biol Chem.</i> 1995 Dec 22;270(51):30749-54.</p> <p>Gong MC, Fuglsang A, Alessi D, Kobayashi S, Cohen P, Somlyo AV, Somlyo AP. Arachidonic acid inhibits myosin light</p> |
| | | | | | <p>chain phosphatase and sensitizes smooth muscle to calcium. <i>J Biol Chem.</i> 1992 Oct 25;267(30):21492-8.</p> <p>Feng J, Ito M, Kureishi Y, Ichikawa K, Amano M, Isaka N, Okawa K, Iwamatsu A, Kaibuchi K, Hartshorne DJ, Nakano T. Rho-associated kinase of chicken gizzard smooth muscle. <i>J Biol Chem.</i> 1999 Feb 5;274(6):3744-52.</p> <p>Katayama T, Watanabe M, Tanaka H, Hino M, Miyakawa T, Ohki T, Ye LH, Xie C, Yoshiyama S, Nakamura A, Ishikawa R, Tanokura M, Oiwa K, Kohama K. Stimulatory effects of arachidonic acid on myosin ATPase activity and contraction of smooth muscle via myosin motor domain. <i>Am J Physiol Heart Circ Physiol.</i> 2010 Feb;298(2):H505-14.</p> |
| Gadolinium (III) chloride (Gd³⁺)/ The peptide GsMTx4 from the tarantula venom | Inhibits mechanosensitive ion channels enabling Ca ²⁺ influx via the PM | <p>Gudipaty SA, Lindblom J, Loftus PD, Redd MJ, Edes K, Davey CF, Krishnegowda V, Rosenblatt J. Mechanical stretch triggers rapid epithelial cell division through Piezo1. <i>Nature.</i> 2017 Mar 2;543(7643):118-121.</p> <p>Miyamoto T, Mochizuki T, Nakagomi H, Kira S, Watanabe M, Takayama Y, Suzuki Y, Koizumi S, Takeda M, Tominaga M. Functional role for Piezo1 in stretch-evoked Ca²⁺ influx and ATP release in urothelial cell</p> | 2APB/Xestospongine C (Xesto) | Blocks stretch-activated inositol triphosphate receptors (InsP3Rs) liberating Ca ²⁺ from membranes of the NE/perinuclear ER and provoking actomyosin | <p>Kim TJ, Joo C, Seong J, Vafabakhsh R, Botvinick EL, Berns MW, Palmer AE, Wang N, Ha T, Jakobsson E, Sun J, Wang Y. Distinct mechanisms regulating mechanical force-induced Ca²⁺ signals at the plasma membrane and the ER in human MSCs. <i>Elife.</i> 2015 Feb 10;4:e04876.</p> <p>Solanes P, Heuzé ML, Maurin M, Bretou M, Lautenschlaeger F, Maiuri P, Terriac E, Thoulouze MI, Launay P, Piel M, Vargas P, Lennon-Duménil AM. Space exploration by dendritic cells requires maintenance of</p> |

| | | | | | |
|--------------|---|--|-----------------|---|--|
| | | cultures. <i>J Biol Chem.</i> 2014 Jun 6;289(23):16565-75. | | activity in a Ca ²⁺ -dependent manner (e.g. via Ca ²⁺ /calmodulin-dependent myosin light chain kinase/MLCK inhibited by the ML-7 compound) | myosin II activity by IP3 receptor 1. <i>EMBO J.</i> 2015 Mar 12;34(6):798-810. Cárdenas C, Liberona JL, Molgó J, Colasante C, Mignery GA, Jaimovich E. Nuclear inositol 1,4,5-trisphosphate receptors regulate local Ca ²⁺ transients and modulate cAMP response element binding protein phosphorylation. <i>J Cell Sci.</i> 2005 Jul 15;118(Pt 14):3131-40. Bootman MD, Fearnley C, Smyrniak I, MacDonald F, Roderick HL. An update on nuclear calcium signalling. <i>J Cell Sci.</i> 2009 Jul 15;122(Pt 14):2337-50. |
| BAPTA | Chelates Ca ²⁺ specifically outside the cell | Solanes P, Heuzé ML, Maurin M, Bretou M, Lautenschlaeger F, Maiuri P, Terriac E, Thoulouze MI, Launay P, Piel M, Vargas P, Lennon-Duménil AM. Space exploration by dendritic cells requires maintenance of myosin II activity by IP3 receptor 1. <i>EMBO J.</i> 2015 Mar 12;34(6):798-810. | BAPTA-AM | Chelates Ca ²⁺ specifically inside the cell | Kono T, Jones KT, Bos-Mikich A, Whittingham DG, Carroll J. A cell cycle-associated change in Ca ²⁺ releasing activity leads to the generation of Ca ²⁺ transients in mouse embryos during the first mitotic division. <i>J Cell Biol.</i> 1996 Mar;132(5):915-23. |

Table S2. Pairwise statistical comparisons related to Fig. 2A

| HeLa-Kyoto cells under the AFM cantilever, 5 μm confinement, myosin II cortex/cytoplasm ratio | |
|---|---|
| Pairwise comparison, perturbation | two-tailed <i>p</i> value, unpaired <i>t</i> test |
| DMSO vs. DOCL (deoxycholate), plasma membrane tension relaxation | <i>p</i> = 0.7920 |
| DMSO vs. Gd^{3+} (GdCl_3), inhibition of mechanosensitive ion channels on the plasma membrane | <i>p</i> = 0.2830 |
| DMSO vs. BAPTA, extracellular Ca^{2+} chelation | <i>p</i> = 0.6368 |
| DMSO vs. AA (AACOCF3), nuclear membrane stretch-sensitive cPLA2 inhibition | <i>p</i> < 0.0001 |
| DMSO vs. 2APB, InsP3R (IP3 receptors - stretch-activated Ca^{2+} channels on the ER) inhibition | <i>p</i> < 0.0001 |
| DMSO vs. BAPTA-AM, intracellular Ca^{2+} chelation | <i>p</i> < 0.0001 |
| DMSO vs. ML7, Ca^{2+} /calmodulin-activated myosin light chain kinase/MLCK inhibition | <i>p</i> < 0.0001 |

| HeLa-Kyoto cells under the AFM cantilever, force response (ΔF , nN) to 5 μm confinement | |
|---|---|
| Pairwise comparison, perturbation | two-tailed <i>p</i> value, unpaired <i>t</i> test |
| DMSO vs. DOCL (deoxycholate), plasma membrane tension relaxation | <i>p</i> = 0.2938 |
| DMSO vs. Gd^{3+} (GdCl_3), inhibition of mechanosensitive ion channels on the plasma membrane | <i>p</i> = 0.7464 |
| DMSO vs. BAPTA, extracellular Ca^{2+} chelation | <i>p</i> = 0.6685 |
| DMSO vs. AA (AACOCF3), nuclear membrane stretch-sensitive cPLA2 inhibition | <i>p</i> < 0.0001 |
| DMSO vs. 2APB, InsP3R (IP3 receptors - stretch-activated Ca^{2+} channels on the ER) inhibition | <i>p</i> = 0.0010 |
| DMSO vs. BAPTA-AM, intracellular Ca^{2+} chelation | <i>p</i> < 0.0001 |
| DMSO vs. ML7, Ca^{2+} /calmodulin-activated myosin light chain kinase/MLCK inhibition | <i>p</i> = 0.0032 |

Table S3. Pairwise statistical comparisons related to Fig. 4G,H

| Melanoma cell chemotaxis through 3D dermal collagen | |
|---|---|
| Pairwise comparison, perturbation | two-tailed <i>p</i> value, unpaired <i>t</i> test |
| DMSO vs. Y27 (Y27632), global actomyosin contractility inhibition | <i>p</i> < 0.0001 |
| DMSO vs. BBS (Blebbistatin), global actomyosin contractility inhibition | <i>p</i> < 0.0001 |
| DMSO vs. AA (AACOCF3), nuclear membrane stretch-sensitive cPLA ₂ inhibition | <i>p</i> < 0.0001 |
| DMSO vs. PA (PACOCF3), nuclear membrane stretch-sensitive cPLA ₂ inhibition | <i>p</i> < 0.0001 |
| <i>Ctrl</i> si vs. <i>PLA2G4A</i> si, treatment with siRNA targeting human cPLA _{2a} | <i>p</i> = 0.0005 |
| <i>Ctrl</i> si vs. <i>LMNA</i> si, treatment with siRNA targeting human lamin A | <i>p</i> = 0.0002 |
| LAP2 vs. LBR OE, stable expression of LAP2b-GFP vs. transient overexpression (OE) of lamin B receptor (LBR) fused to GFP | <i>p</i> = 0.0011 |
| DMSO vs. 2APB, InsP3R (IP3 receptors - stretch-activated Ca^{2+} channels on the ER) inhibition | <i>p</i> < 0.0001 |
| DMSO vs. Xesto (Xestospongine C), InsP3R (IP3 receptors - stretch-activated Ca^{2+} channels on the ER) inhibition | <i>p</i> = 0.0002 |
| DMSO vs. ML7, Ca^{2+} /calmodulin-activated myosin light chain kinase/MLCK inhibition | <i>p</i> = 0.0006 |
| DMSO vs. Gd^{3+} (GdCl_3), inhibition of mechanosensitive ion channels on the plasma membrane | <i>p</i> = 0.6054 |
| DMSO vs. GsMTx4 (Tarantula venom peptide), inhibition of mechanosensitive ion channels on the plasma membrane | <i>p</i> = 0.6697 |

| Melanoma cell transmigration through 12 μm pores | |
|---|---|
| Pairwise comparison, perturbation | two-tailed <i>p</i> value, unpaired <i>t</i> test |
| DMSO vs. Y27 (Y27632), global actomyosin contractility inhibition | <i>p</i> = 0.0112 |
| DMSO vs. BBS (Blebbistatin), global actomyosin contractility inhibition | <i>p</i> = 0.0257 |
| DMSO vs. AA (AACOCF3), nuclear membrane stretch-sensitive cPLA2 inhibition | <i>p</i> = 0.6381 |
| DMSO vs. PA (PACOCF3), nuclear membrane stretch-sensitive cPLA2 inhibition | <i>p</i> = 0.3806 |
| <i>Ctrl</i> si vs. <i>PLA2G4A</i> si, treatment with siRNA targeting human cPLA _{2a} | <i>p</i> = 0.6207 |
| <i>Ctrl</i> si vs. <i>LMNA</i> si, treatment with siRNA targeting human lamin A | <i>p</i> = 0.0544 |
| LAP2 vs. LBR OE, stable expression of LAP2b-GFP vs. transient overexpression (OE) of lamin B receptor (LBR) fused to GFP | <i>p</i> = 0.3591 |
| DMSO vs. 2APB, InsP3R (IP3 receptors - stretch-activated Ca^{2+} channels on the ER) inhibition | <i>p</i> = 0.3578 |
| DMSO vs. Xesto (Xestospongine C), InsP3R (IP3 receptors - stretch-activated Ca^{2+} channels on the ER) inhibition | <i>p</i> = 0.7148 |
| DMSO vs. ML7, Ca^{2+} /calmodulin-activated myosin light chain kinase/MLCK inhibition | <i>p</i> = 0.6993 |
| DMSO vs. Gd^{3+} (GdCl_3), inhibition of mechanosensitive ion channels on the plasma membrane | <i>p</i> = 0.0680 |
| DMSO vs. GsMTx4 (Tarantula venom peptide), inhibition of mechanosensitive ion channels on the plasma membrane | <i>p</i> = 0.6241 |

| Melanoma cell transmigration through 8 μm pores | |
|---|---|
| Pairwise comparison, perturbation | two-tailed <i>p</i> value, unpaired <i>t</i> test |
| DMSO vs. Y27 (Y27632), global actomyosin contractility inhibition | <i>p</i> < 0.0001 |
| DMSO vs. BBS (Blebbistatin), global actomyosin contractility inhibition | <i>p</i> < 0.0001 |
| DMSO vs. AA (AACOCF3), nuclear membrane stretch-sensitive cPLA2 inhibition | <i>p</i> < 0.0001 |
| DMSO vs. PA (PACOCF3), nuclear membrane stretch-sensitive cPLA2 inhibition | <i>p</i> < 0.0001 |
| <i>Ctrl</i> si vs. <i>PLA2G4A</i> si, treatment with siRNA targeting human cPLA _{2a} | <i>p</i> = 0.0006 |
| <i>Ctrl</i> si vs. <i>LMNA</i> si, treatment with siRNA targeting human lamin A | <i>p</i> = 0.0004 |
| LAP2 vs. LBR OE, stable expression of LAP2b-GFP vs. transient overexpression (OE) of lamin B receptor (LBR) fused to GFP | <i>p</i> = 0.0005 |
| DMSO vs. 2APB, InsP3R (IP3 receptors - stretch-activated Ca^{2+} channels on the ER) inhibition | <i>p</i> < 0.0001 |
| DMSO vs. Xesto (Xestospongine C), InsP3R (IP3 receptors - stretch-activated Ca^{2+} channels on the ER) inhibition | <i>p</i> = 0.0053 |
| DMSO vs. ML7, Ca^{2+} /calmodulin-activated myosin light chain kinase/MLCK inhibition | <i>p</i> = 0.0061 |
| DMSO vs. Gd^{3+} (GdCl_3), inhibition of mechanosensitive ion channels on the plasma membrane | <i>p</i> = 0.0568 |
| DMSO vs. GsMTx4 (Tarantula venom peptide), inhibition of mechanosensitive ion channels on the plasma membrane | <i>p</i> = 0.9382 |

Movie S1.

Rounded nonadherent HeLa-Kyoto cells sense the difference between 10 and 5 μm confinement – spatially confining cells to 5 but not 10 μm height stimulates rapid recruitment of myosin II from the cytosol to the cortex. Left, a representative cell expressing MYH9-GFP (pseudocolored using the thermal LUT mode with hot and cold tones indicating high and low levels of MYH9-GFP fluorescence signal respectively) immediately after the 10 μm height is reached. Right, the same cell after 5 μm confinement. Time interval between consecutive images, 5 s. Scale bar, 5 μm .

Movie S2.

Rounded nonadherent HeLa-Kyoto cells undergo a discrete morphodynamic switch from a noncontractile cell cortex and filopodia formation to a highly contractile cortex and vigorous plasma membrane blebbing in response to 10-to-5 μm confinement. Left, a representative cell expressing MYH9-GFP (pseudocolored in magenta) and LifeAct-mCherry (pseudocolored in cyan) during 20-to-10 μm confinement. Right, the same cell during 10-to-5 μm confinement. A differential-interference-contrast (DIC) image of the confining flat microcantilever is shown in the grey channel. Time interval between consecutive images, 5 s. Scale bar, 5 μm .

Movie S3.

Rounded nonadherent HeLa-Kyoto cells expand their nuclei and unfold the nuclear envelope prior to the onset of the contractile cell response manifested in active plasma membrane blebbing during 10-to-5 μm confinement. The representative cell expresses LAP2-GFP as a marker of the nuclear envelope (green) and is stained with the SiR-actin probe to reveal F-actin (pseudocolored in magenta). The cell was confined from 20-to-10-to-5 μm . The video is artificially paused several times during the 10-to-5 μm transition to accentuate nuclear expansion-unfolding taking place before the cell retracts the very first rounded blebs. These structures represent passive bleb-like protrusions appearing upon physical squeezing of the cell (i.e. when intracellular fluid is pushed against the plasma membrane through pre-existing cracks in the cell cortex). Our additional observations (data not shown) reveal that such “passive” blebs almost instantaneously accumulate submembranous cortical F-actin. The cortex of the “passive” blebs gets retracted by active myosin II motors initiating a continuous active blebbing. “Active” blebs are more numerous, often of a larger length, and significantly smaller in width compared to their “passive” counterparts. Time interval between consecutive images, 5 s. Scale bar, 5 μm .

Movie S4.

Rounded nonadherent, enucleated HeLa-Kyoto cells (cytoplasts) do not sense the difference between confinement heights relevant to the contractile response in nucleated cells. Left, a representative nucleated cell expressing MYH9-GFP (pseudocolored in magenta) and LifeAct-mCherry (pseudocolored in cyan) that survived the treatments and centrifugation protocol required for enucleated cytoplast generation. Right, a representative enucleated cytoplast. The video starts from depicting a nonconfined state of these cells followed by 20-to-10-to-5 μm confinement. Note, despite its smaller size (height), the nucleated cell that survived the cytoplast generation protocol initiates the sustained, active contractile response (cortical accumulation of myosin II and vigorous plasma membrane blebbing) right before the confining cantilever stops at 5 μm during the

movement from 10 to 5 μm . However, the enucleated cytoplasm displays only a passive response in the form of transient bleb-like protrusions generated due to physical squeezing of the cytoplasm during the 10-to-5 μm confinement. Time interval between consecutive images, 5 s. Scale bar, 5 μm .

Movie S5.

Compression of the cell cortex down to 0.5 μm confinement height yields only local and highly transient bleb-like protrusions without any global effect on the levels of actomyosin contractility. Left, a representative spread adherent HeLa-Kyoto cell expressing MYH9-GFP (pseudocolored in magenta), LifeAct-mCherry (pseudocolored in cyan) and additionally stained with DAPI (pseudocolored in yellow). A differential-interference-contrast (DIC) image of the confining flat microcantilever is shown in the grey channel. The precise position of the cantilever was adjusted such that only the lamellar but not organelle-rich compartment is engaged in the local cell compression. Right, a time-lapse video of the cell responding to strong local cortical compression (500 nm confinement). Time interval between consecutive images, 5 s. Scale bar, 10 μm .

Movie S6.

Induction of the global sustained contractile cell response to local nuclear but not cortex/cytoplasm confinement. The video depicts representative spread adherent HeLa-Kyoto cells expressing MYH9-GFP (pseudocolored in magenta), LifeAct-mCherry (pseudocolored in cyan) and additionally stained with DAPI (pseudocolored in yellow) to reveal the nuclear compartment. A differential-interference-contrast (DIC) image of the confining flat microcantilever is shown in the grey channel. The precise position of the cantilever was adjusted such that only the nuclear compartment of the lower cell and the lamellar region of the upper cell are engaged in the local confinement. Confinement height, 2 μm . Note, while local cortex/cytoplasm confinement produces local, short-lived bleb-like protrusions (passive response to physical compression), local nuclear-specific confinement results in a global, sustained increase in cell contractility even in the non-confined cell region that switches to this state with a delay (activation signal propagation). Time interval between consecutive images, 5 s. Scale bar, 10 μm .

Movie S7.

Populations of LifeAct-GFP-expressing immature dendritic cells (iDCs) subjected to confinement in microfabricated devices. Primary bone marrow-derived iDCs from LifeAct-GFP mice were treated with control siRNA or siRNA targeting cPLA2a. The cells were separately confined to 4 and 3 μm heights and imaged using fluorescence videomicroscopy. Time interval between consecutive images, 2 min. Scale bar, 25 μm .